



2

AD-A247 037

SSS-TR-90-12132



**Effects of Subduction Zone Structure on
the Propagation of Explosion-Generated
Long-Period Rayleigh Waves**



**K. L. McLaughlin
T. G. Barker
S. M. Day
B. Shkoller
J. L. Stevens**

Technical Report

CDRL 003A2

**Sponsored by:
DEFENSE ADVANCED RESEARCH PROJECTS AGENCY**

**Monitored by:
U.S. AIR FORCE TECHNICAL APPLICATIONS CENTER
Under Contract No. F08606-89-C-0022**

This document has been approved
for public release and sale; its
distribution is unlimited.

January 1991

**P. O. Box 1620, La Jolla, California 92038-1620
(619) 453-0060**

92-05166



92 2 28 036

REPORT DOCUMENTATION PAGE			Form Approved OMB No. 0704-0188	
<small>Public reporting burden for this collection of information is estimated to average 1 hour per response, including the time for reviewing instructions, searching existing data sources, gathering and maintaining the data needed, and completing and reviewing the collection of information. Send comments regarding this burden estimate or any other aspect of this collection of information, including suggestions for reducing this burden, to Washington Headquarters Services, Directorate for Information Operations and Reports, 1215 Jefferson Davis Highway, Suite 1204, Arlington VA 22202-4302, and to the Office of Management and Budget, Paperwork Reduction Project (0704-0188), Washington, DC 20503.</small>				
1. AGENCY USE ONLY (Leave blank)		2. REPORT DATE January 1991		3. REPORT TYPE AND DATES COVERED Technical Report
4. TITLE AND SUBTITLE Effects of Suduction Zone Structure on the Propagation of Explosion-Generated Long-Period Rayleigh Waves			5. FUNDING NUMBERS C - F08606-89-C-0022	
6. AUTHOR(S) K. L. McLaughlin, T. G. Barker, S. M. Day, B. Shkoller and J. L. Stevens				
7. PERFORMING ORGANIZATION NAME(S) AND ADDRESS(ES) S-CUBED, A Division of Maxwell Laboratories, Inc. P.O. Box 1620 La Jolla, CA 92038-1620			8. PERFORMING ORGANIZATION REPORT NUMBER SSS-TR-90-12132	
9. SPONSORING/MONITORING AGENCY NAME(S) AND ADDRESS(ES) Defense Advanced Research Projects Agency 3701 N. Fairfax, Suite 717 Arlington, VA 22209-1714			10. SPONSORING/MONITORING AGENCY REPORT NUMBER	
11. SUPPLEMENTARY NOTES				
12a. DISTRIBUTION/AVAILABILITY STATEMENT Approved for public release; distribution is unlimited.			12b. DISTRIBUTION CODE	
13. ABSTRACT (Maximum 200 words) 3D linear elastic finite difference calculations were used to investigate effects of near-source scattering on long-period surface waves radiated by shallow explosions located in the arc of subduction zone. A 3D velocity model was constructed based on the Aleutian subduction zone structure of Boyd and Creager (1991) and crustal refraction results reported by Lambert, <i>et al.</i> (1970). Each finite difference grid consisted of 2 million nodes and the calculations were designed to model surface waves in the 20 to 40 second period range at distances up to 400 km from the source. Displacements on the free surface were analyzed to show the effects of the velocity structure upon the 3D propagation of Rayleigh waves from an explosion source. Azimuthally dependent Rayleigh wave amplitudes are clearly seen as well as Rayleigh-to-Love wave conversion along the strike of the subduction zone structures. Teleseismic Rayleigh wave amplitude anomalies of up to a factor of two are clearly evident from the near-source scattering. Love waves 1/3 to 1/4 the amplitude of the Rayleigh waves are radiated in narrow azimuthal ranges.				
14. SUBJECT TERMS Surface Waves Finite Difference Amchitka Explosion Seismology Subduction Zone Rayleigh Waves			15. NUMBER OF PAGES 60	
			16. PRICE CODE	
17. SECURITY CLASSIFICATION OF REPORT Unclassified	18. SECURITY CLASSIFICATION OF THIS PAGE Unclassified	19. SECURITY CLASSIFICATION OF ABSTRACT Unclassified	20. LIMITATION OF ABSTRACT	

UNCLASSIFIED

SECURITY CLASSIFICATION OF THIS PAGE

CLASSIFIED BY:

DECLASSIFY ON:

SECURITY CLASSIFICATION OF THIS PAGE

UNCLASSIFIED

TABLE OF CONTENTS

<u>SECTION</u>	<u>PAGE</u>
Abstract	vii
1 Introduction	1
2 Tectonic Release Versus Propagation Effects	2
3 3D Finite Difference Methods	14
4 The Model	15
5 Analysis and Discussion	20
Acknowledgements	47
References	48
Appendix I: Use of the Surface-Wave Fresnel-Kirchoff Integral with Finite Difference Calculations	51
Distribution List	57



Accession For	
NTIS CRA&I	<input checked="" type="checkbox"/>
DTIC TAB	<input type="checkbox"/>
Unannounced	<input type="checkbox"/>
Justification	
By	
Distribution /	
Availability Codes	
Dist	Avail and/or Special
A-1	

LIST OF ILLUSTRATIONS

FIGURE	PAGE
1 Path-corrected long-period Rayleigh-wave (LR) amplitudes from Stevens and McLaughlin (1989) for explosions LONGSHOT, MILROW, and CANNIKIN located at the Amchitka test site.	3
2. Radiation patterns for CANNIKIN (top), MILROW (middle), and LONGSHOT (bottom) inferred from path corrected Rayleigh wave amplitudes.	4
3. Ms station magnitudes for CANNIKIN (circles) and MILROW (triangles) from Willis, et al. (1972).....	6
4. Normalized station amplitudes for CANNIKIN from Willis, et al. (1972).	7
5. MILROW explosion and collapse Ms station magnitudes from von Seggern and Lambert (1972).....	9
6. MILROW station explosion minus collapse Ms.....	10
7. Maximum likelihood station effects for Ms magnitudes read at WWSSN stations from LONGSHOT, MILROW, and CANNIKIN.....	11
8. The 3D finite difference grid was oriented with the v axis aligned north, u axis east and z axis down.	16
9. Map of region around Amchitka Island test site showing the approximate location of the trench axis and an 840 by 840 km box representing the finite difference grid used in the simulations.	17
10. Contours of the S-wave velocity field along the north-south vertical plane.....	19
11A. Contours of displacement amplitude of the vertical, radial, and transverse components of motion on the free-surface of the finite difference grid at time $t = 70$ seconds.....	21
11B. Contours of displacement amplitude of the vertical, radial, and transverse components of motion on the free-surface of the finite difference grid at time $t = 100$ seconds.....	22
11C. Contours of displacement amplitude of the vertical, radial, and transverse components of motion on the free-surface of the finite difference grid at time $t = 130$ seconds.....	23

LIST OF ILLUSTRATIONS (CONTINUED)

FIGURE	PAGE
11D. Contours of displacement amplitude of the vertical, radial, and transverse components of motion on the free-surface of the finite difference grid at time $t = 150$ seconds.....	24
12. Wavenumber spectra at 0.047 Hz from a synthetic array of stations located 300 km from the source at an azimuth of 68 degrees	25
13. Wavenumber spectra at 0.047 Hz from a synthetic array of stations located 300 km from the source at an azimuth of 160 degrees	26
14A. Vertical component of motion displayed for a constant distance from the source, 270 km, as a function of time and azimuth.....	28
14B. Radial component of motion displayed for a constant distance from the source, 270 km, as a function of time and azimuth, same scale as vertical components.	29
14C. Transverse component of motion displayed for a constant distance from the source, 270 km, as a function of time and azimuth, 5X scale as vertical/radial components	30
15 Peak bandpass filtered Rayleigh wave (LR) amplitude (periods of 20 and 30 sec) as a function of azimuth at a distance of 300 km from the source	31
16 Peak 20 and 30 second Rayleigh wave amplitude at 350 km from the source (bottom) and the arrival time (top) for simulation 3D#1	32
17A. Contours of peak LR amplitude at 0.05 Hz from simulation 3D#1.....	34
17B. Contours of peak LR amplitude at 0.05 Hz from 3D simulation 3D#1, corrected for $1/\sqrt{R}$ geometrical spreading	35
18A. Contours of peak LR amplitude at 0.05 Hz from simulation 3D#2.	36
18B. Contours of peak LR amplitude at 0.05 Hz from simulation 3D#2, corrected for $1/\sqrt{R}$ geometrical spreading.	37

LIST OF ILLUSTRATIONS (CONTINUED)

<u>FIGURE</u>	<u>PAGE</u>
19A. The relative amplitude (bottom) and phase (top) for the Rayleigh wave at a distance of 300 km from the source in 3D simulation #1	39
19B. The relative amplitude (bottom) and phase (top) for the Rayleigh wave at a distance of 370 km from the source in 3D simulation #2.....	40
20A. Predicted teleseismic amplitudes from 3D simulation #1 as a function of azimuth using the Fresnel-Kirchoff integral to account for diffraction effects in the far-field.....	41
20B. Predicted teleseismic amplitudes from 3D simulation #2 as a function of azimuth using the Fresnel-Kirchoff integral to account for diffraction effects in the far-field.....	42

ABSTRACT

3D linear elastic finite difference calculations were used to investigate effects of near-source scattering on long-period surface waves radiated by shallow explosions located in the arc of a subduction zone. These simulations were motivated by the teleseismic Rayleigh-wave amplitude patterns of explosions detonated at the Amchitka test site. Amplitude patterns of these explosion-generated 20-40 second surface waves show evidence of both tectonic release and source-receiver path effects.

A 3D velocity model was constructed based on the Aleutian subduction zone structure of Boyd and Creager (1991) and crustal refraction results reported by Lambert, *et al.* (1970). Two 3D finite difference calculations were performed to assess the sensitivity of the results to the source location and fine details of the velocity model. Each finite difference grid consisted of 2 million nodes and the calculations were designed to model surface waves in the 20 to 40 second period range at distances up to 400 km from the source.

Displacements on the free surface were analyzed to show the effects of the velocity structure upon the 3D propagation of Rayleigh waves from an explosion source. Azimuthally dependent Rayleigh wave amplitudes are clearly seen as well as Rayleigh-to-Love wave conversion along the strike of the subduction zone structures. Teleseismic Rayleigh wave amplitude anomalies of up to a factor of two are clearly evident from the near-source scattering. Love waves $1/3$ to $1/4$ the amplitude of the Rayleigh waves are radiated in narrow azimuthal ranges.

A method for the continued propagation of surface waves is presented based on a 2D Fresnel-Kirchoff integral for surface waves. The Fresnel-Kirchoff integral accounts for diffraction effects assuming uniform propagation outside the finite difference grid. This hybrid procedure using both the finite difference simulation and the Fresnel-Kirchoff integral predicts 50% Rayleigh wave amplitude anomalies at teleseismic distances due to structure within 400 km of the Amchitka test site.

I. INTRODUCTION

Detailed aspects of the Rayleigh wave radiation from the three Amchitka explosions, LONGSHOT, MILROW, and CANNIKIN, have remained a problem since the early 1970's. The Rayleigh-wave amplitudes from these events show evidence for both tectonic release and nonisotropic source-receiver propagation effects. The evidence is clear that the large events were accompanied by tectonic release. However, there has remained questions as to how much of the apparent radiation pattern from the three Amchitka explosions is due to tectonic release and how much is due to source-receiver propagation effects. Since Amchitka Island lies above an active subduction zone, the possibility has remained that the complex near-source structure introduced an apparent radiation pattern observed at teleseismic distances. In this study, we model the long-period surface-wave propagation in the near-source subduction zone structure around Amchitka Island and examine the potential nonisotropic propagation effects on Rayleigh and Love waves from isotropic explosion sources. Three dimensional linear elastic finite difference calculations were performed to model the complete wave propagation effects for periods longer than 20 seconds. The results from these calculations are compared to observed Rayleigh and Love waves from the three Amchitka explosions.

2. TECTONIC RELEASE VERSUS PROPAGATION EFFECTS

In order to reduce systematic errors due to path structure and put the estimation of long-period underground explosion source characteristics in the form of a physically meaningful quantity such as the seismic moment tensor, the method of Rayleigh wave path correction was introduced (Stevens, 1986a). Rayleigh and Love waves from the test site are used to derive an average structure between the test site and each station in the network. The Rayleigh and Love wave amplitude and phase (normal or reversed) is then used to estimate a moment tensor for the explosion plus tectonic release (Given and Mellman, 1986; Stevens, 1986a). Unfortunately, the path corrections can only partially correct for the effects of propagation between the source and receivers. There remain propagation effects due to the laterally heterogeneous structure of the Earth. These remaining propagation effects result in individual station corrections. It has been found that a trade-off exists between the determination of a tectonic release pattern for events at the test site and the average station correction pattern for the network of stations. Residual propagation effects can be mistaken for a tectonic release pattern and vice versa.

Figure 1 shows the average station corrections determined from the three Amchitka events assuming that the log of all station correction factors sum to zero (Stevens and McLaughlin, 1989). Rather than showing a random azimuthal pattern, the station corrections exhibit a strong trend from large amplitudes to small amplitudes between azimuths of 40 and 70 degrees. Fits to the Rayleigh wave amplitudes for CANNIKIN, MILROW, and LONGSHOT are shown in Figure 2 from Stevens and McLaughlin (1989) with F factors (ratio of isotropic to double-couple moment) ranging between 0.2 and 0.3. Note that the inferred tectonic release patterns are strongly influenced by the low amplitudes to the east and large amplitudes to the north-east as seen (inversely) in the station corrections.

This azimuthal radiation pattern has been studied with interest since the earliest analysis of surface waves from the Amchitka test site. Researchers have compared Rayleigh waves from different explosions as well as Rayleigh to Love wave ratios, and studied Rayleigh waves from explosion cavity collapses in order to estimate the effects of propagation on the Rayleigh wave amplitudes

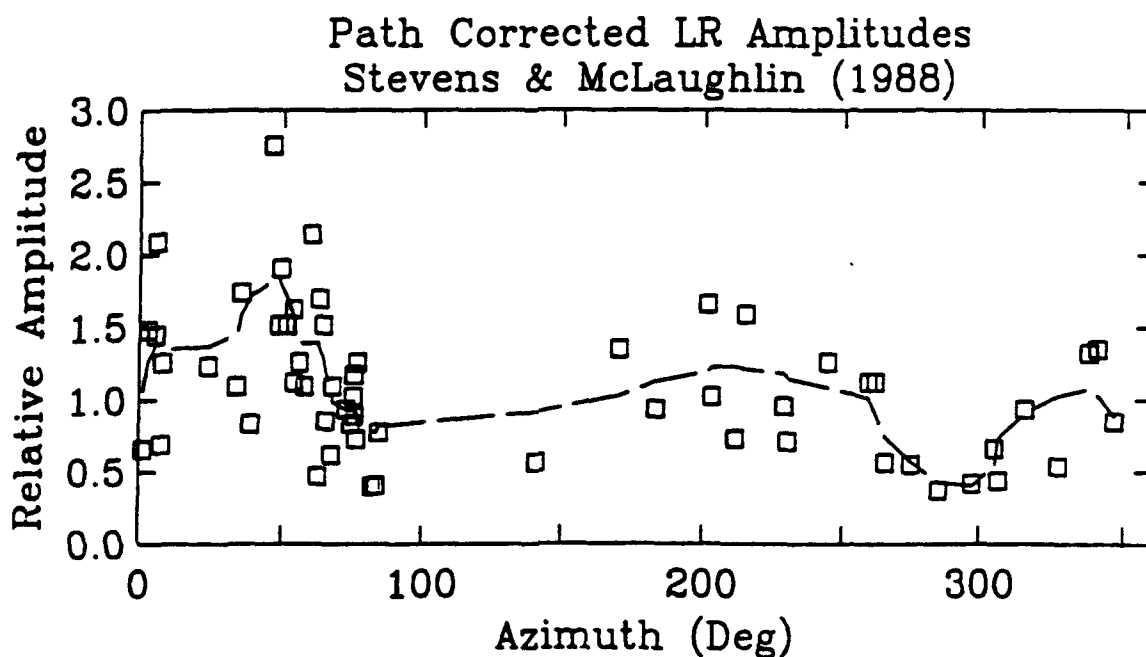
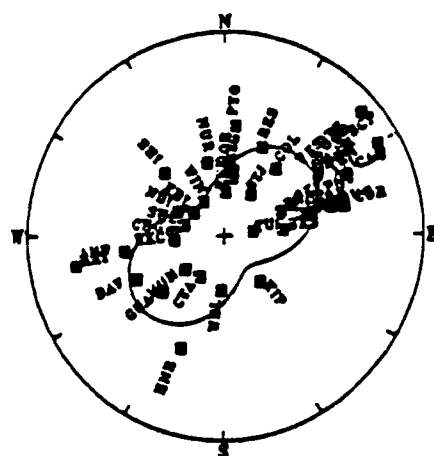


Figure 1. Path-corrected long-period Rayleigh-wave (LR) amplitudes from Stevens and McLaughlin (1989) for explosions LONGSHOT, MILROW, and CANNIKIN located at the Amchitka test site. Note the trend from large amplitudes between 40 and 60 degrees to small amplitudes between 60 and 90 degrees. A nonparametric smoother has been applied to the data (dashed line).

Amchitka Radiation Patterns

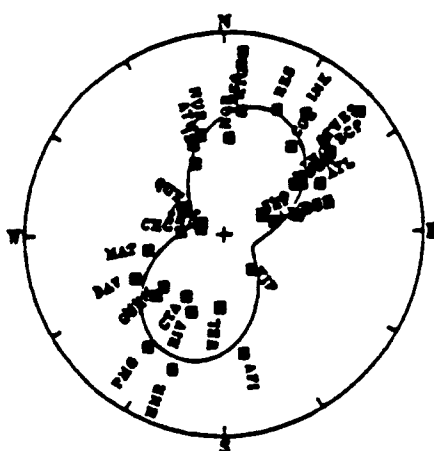


Cannikin

$$\text{Log } M_0 = 17.83 \pm 0.18$$

$$F = 0.21$$

$$\text{Strike} = 7^\circ$$

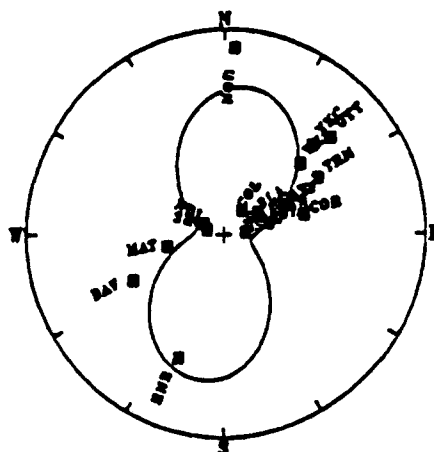


Milrow

$$\text{Log } M_0 = 17.14 \pm 0.21$$

$$F = 0.27$$

$$\text{Strike} = 337^\circ$$



Longshot

$$\text{Log } M_0 = 16.08 \pm 0.29$$

$$F = 0.30$$

$$\text{Strike} = 326^\circ$$

Figure 2. Radiation patterns for CANNIKIN (top), MILROW (middle), and LONGSHOT (bottom) inferred from path corrected Rayleigh wave amplitudes. The trend of large amplitudes in the north-east to small amplitudes in the east result in radiation patterns with a minimum to the east-southeast for each event. The ratios of double-couple to isotropic moment range from 0.2 to 0.3 for the three events.

used to estimate the surface wave magnitude, (M_s) and moments of these explosions.

Willis, *et al.* (1972) and Toksoz and Kehrler (1972) both studied the Rayleigh and Love waves radiated by CANNIKIN. Toksoz and Kehrler concluded from an analysis of Rayleigh/Love wave ratios that CANNIKIN was accompanied by tectonic release ($F = 0.4$) with an isotropic moment of 5×10^{17} Nt-m. Both studies noted the large Rayleigh wave amplitudes across the Canadian network (azimuths 10 to 70 deg), which are only partly explained by a tectonic release model. In addition, Willis, *et al.* examined Rayleigh wave amplitudes from the MILROW explosion and the CANNIKIN collapse. The individual MILROW and CANNIKIN M_s values in the first quadrant (0-90 deg) from Willis, *et al.* are shown in Figure 3. There is a strong gradient in Rayleigh wave amplitude of nearly 0.5 magnitude units between 40 and 70 degrees. The radiation pattern proposed by Toksoz and Kehrler from an explosion plus double-couple Rayleigh-wave radiation pattern is shown for comparison (dotted line). Note the similarity of the apparent radiation pattern between the two events suggesting a common cause(s) for the amplitude patterns.

In Figure 4, we show the CANNIKIN Rayleigh wave amplitudes (from Willis, *et al.*) normalized to Rayleigh wave amplitudes from the CANNIKIN collapse event. It is often assumed that a collapse is an axisymmetric source so the ratio of explosion to collapse amplitudes should cancel propagation and instrumental effects that otherwise complicate interpretation of Rayleigh wave amplitudes (Masse, 1971). The normalized Rayleigh waves show a distinct azimuthal pattern that is partially fit by the theoretical radiation pattern of an explosion plus a double-couple due to Toksoz and Kehrler.

Also comparing explosions and collapses, von Seggern (1973) concluded from a study of MILROW, MILROW collapse, and LONGSHOT Love waves that a mechanism(s) other than tectonic release contributed to Love waves for these events. He used matched filters derived from MILROW's Love waves to isolate the Love waves excited by MILROW collapse and the LONGSHOT explosion. Assuming the collapse was axisymmetric, it should not excite Love waves. Furthermore, the ratio of Love wave amplitudes between MILROW and LONGSHOT are consistent with the yield scaling between the two

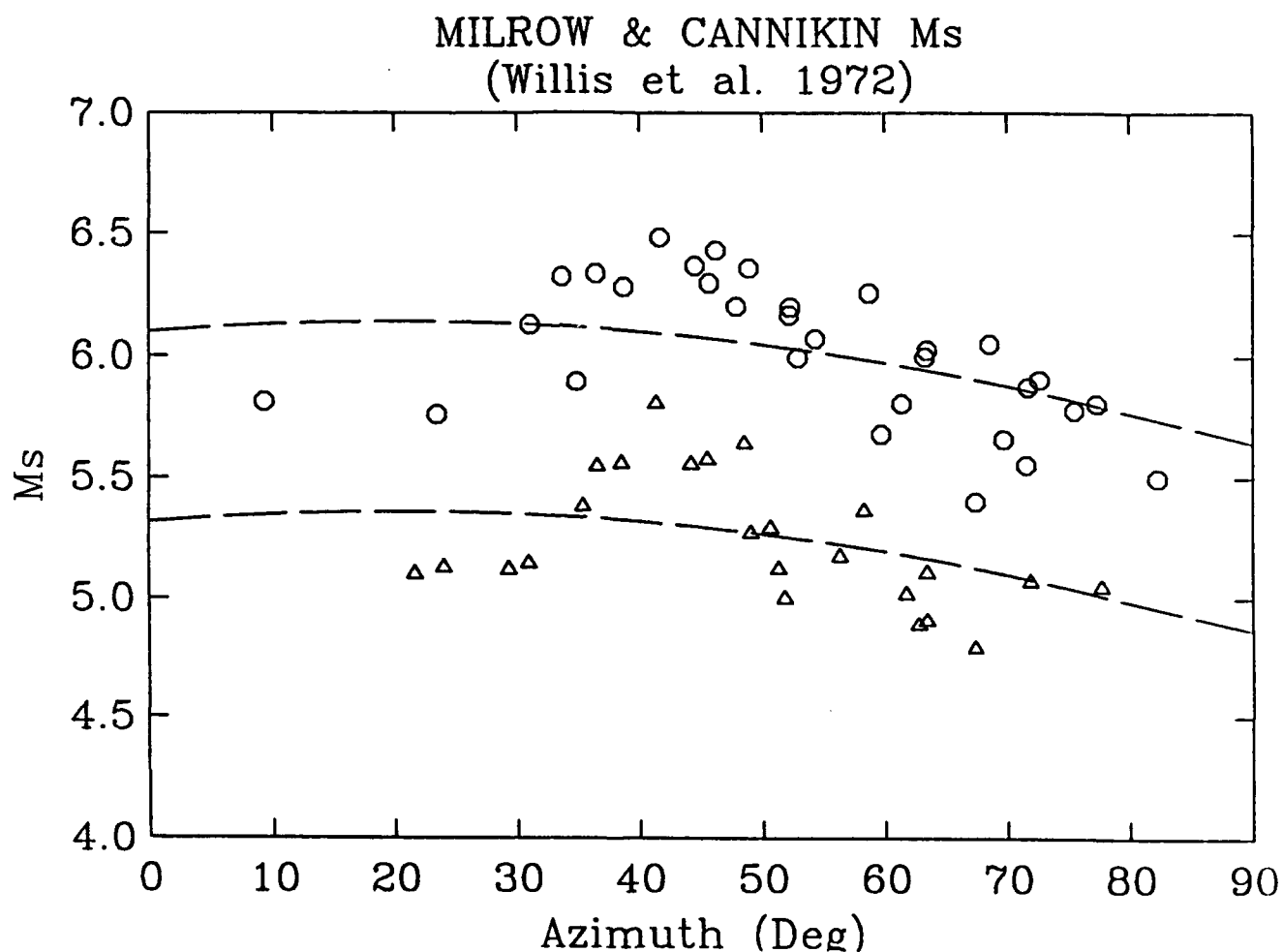


Figure 3. Ms station magnitudes for CANNIKIN (circles) and MILROW (triangles) from Willis, *et al.* (1972). The radiation pattern from Toksoz and Kehrner (1972) is superimposed on the two data sets (dashed line). Note the trend in large to small magnitudes between 40 and 90 degrees azimuth.

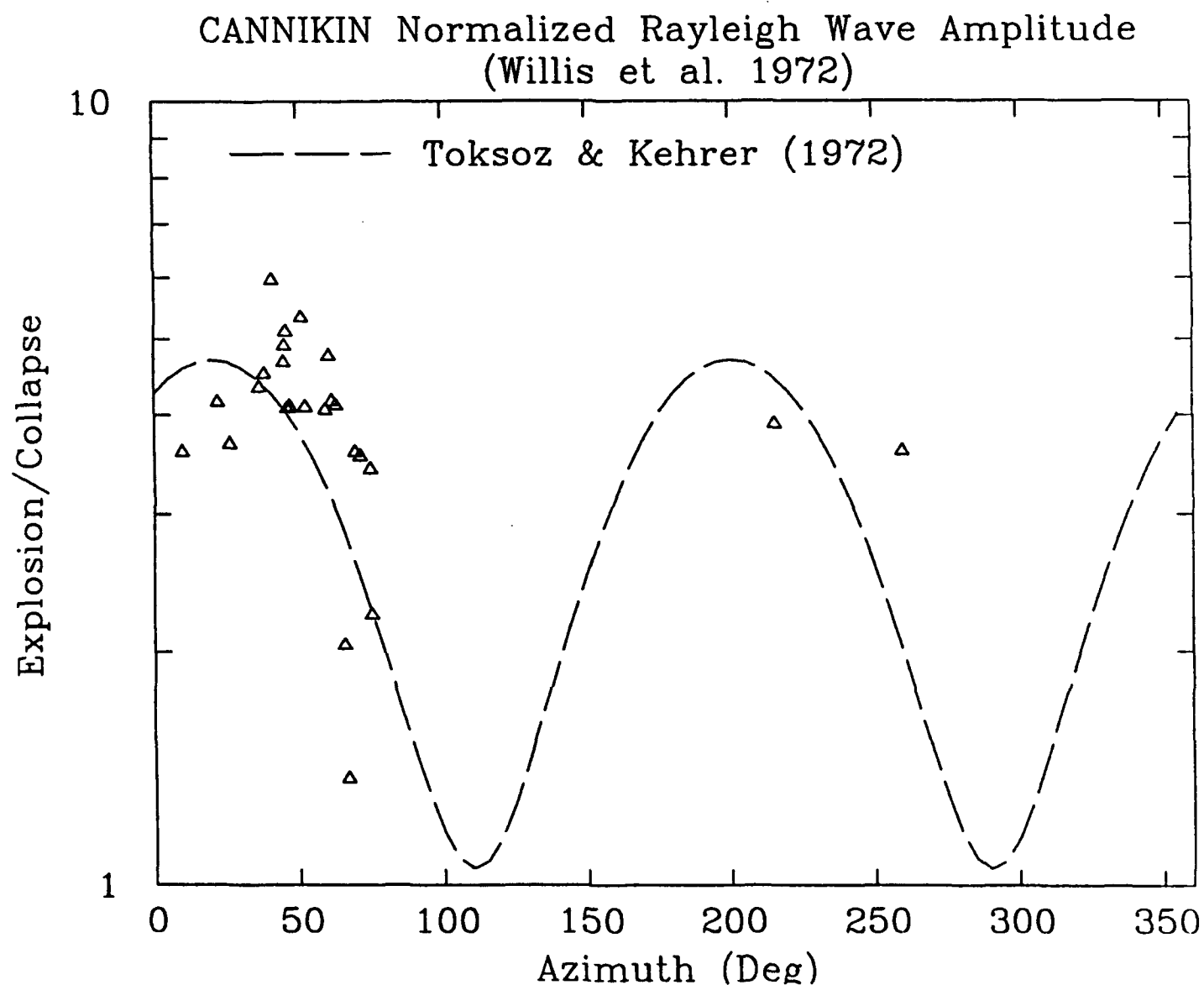


Figure 4. Normalized station amplitudes for CANNIKIN from Willis, *et al.* (1972). The radiation pattern from Toksoz and Kehrner (1972) is superimposed (dashed line). Note the trend in large to small magnitudes between 40 and 90 degrees azimuth is only partially modeled by the tectonic release pattern.

events, suggesting that Love wave excitation was proportional to the explosion part of the source. If the collapses are axisymmetric sources, then von Seggern's observations are consistent with the hypothesis that the MILROW and LONGSHOT Love waves were produced by scattering of Rayleigh waves to Love waves along the propagation path.

Figure 5 shows the MILROW explosion and collapse Ms magnitudes from von Seggern and Lambert (1972). The amplitude pattern is similar to Ms data of Willis, *et al.* in Figure 4 for both the explosion and the collapse. Figure 6 shows the MILROW Ms difference (explosion - collapse) at common stations in the first quadrant. No statistically significant trend is present in the Ms difference between 40 and 90 degrees. This evidence suggests that the MILROW explosion and collapse have a similar radiation pattern. If the MILROW collapse is an isotropic source then it appears that most of the MILROW explosion radiation pattern is path related and not tectonic release.

The results of von Seggern's analysis suggest strong near-source propagation effects that affect both explosion and collapse Rayleigh and Love excitation. Since the subduction zone structure near Amchitka Island has a reflection symmetry about a north-south plane, a scattering hypothesis would predict a reflection symmetry in the Rayleigh wave radiation pattern about a north-south axis. The maximum likelihood WWSSN Ms station corrections from McLaughlin, *et al.* (1986) are plotted in Figure 7 as a function of azimuth. This study utilized a large number of WWSSN stations for all three Amchitka Island events at azimuths not used in some other studies. The station effects are plotted from 0 to 360 deg azimuth in the lower panel. Note the dip in station effects near 270 degrees is similar to the dip near 90 degrees. In the upper panel, stations between 180 and 360 degrees are plotted at 360 minus the azimuth as would be suggested by a reflection symmetry about a north-south line. It appears from Figure 7 that the WWSSN Ms station effects are consistent with a north-south reflection symmetry but because of the paucity of stations between 90 and 180 degrees it is not a completely convincing test.

It is interesting that based on data from collapse events, Willis, *et al.* (1972) concluded that CANNIKIN is contaminated by tectonic release while von Seggern concluded that the structural effect rather than tectonic release is the

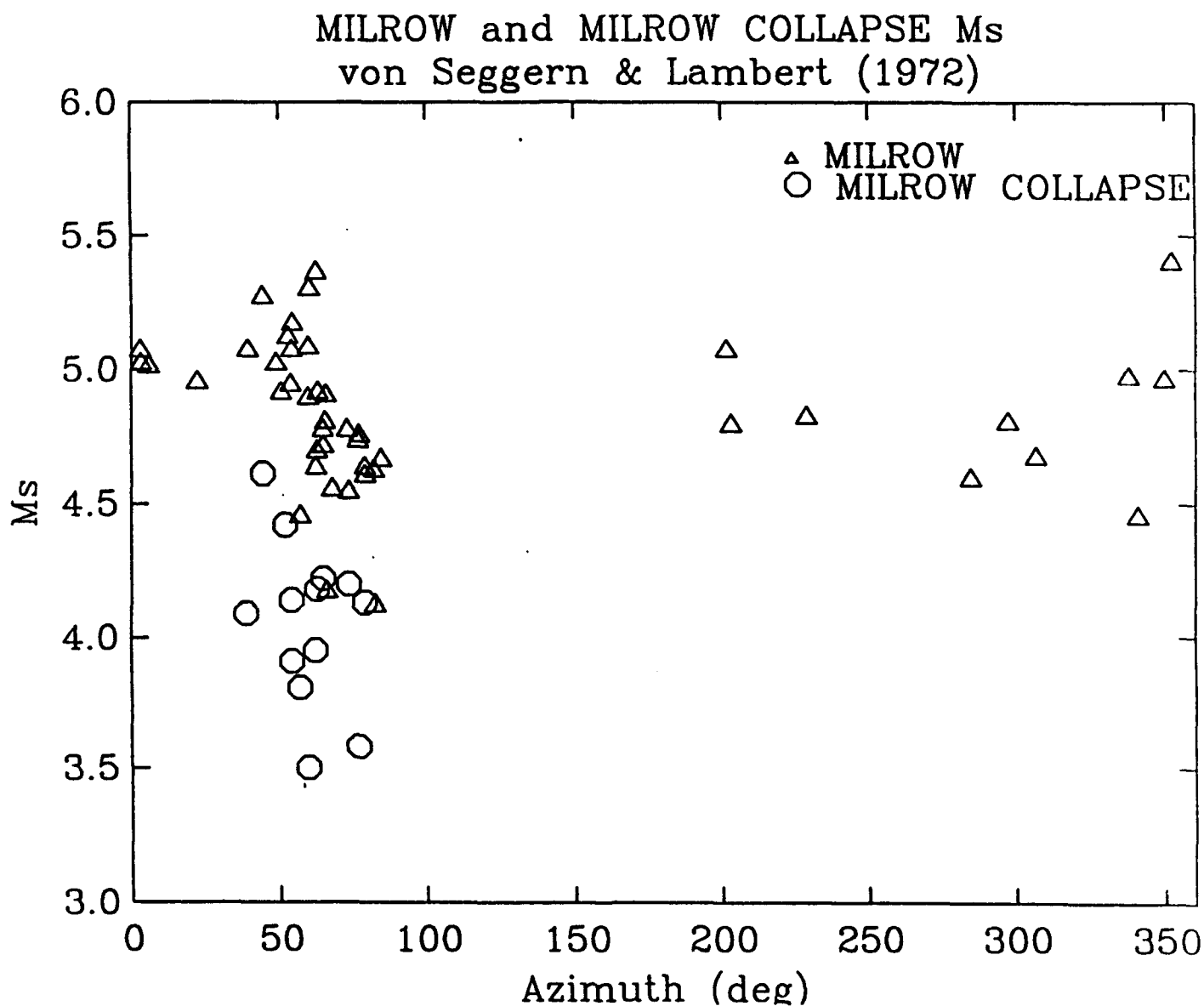


Figure 5. MILROW explosion and collapse M_s station magnitudes from von Seggern and Lambert (1972). The explosion (triangles) and collapse (circles) magnitudes show the same trend between 40 and 90 degrees azimuth. Data from the collapse is limited to the first quadrant.

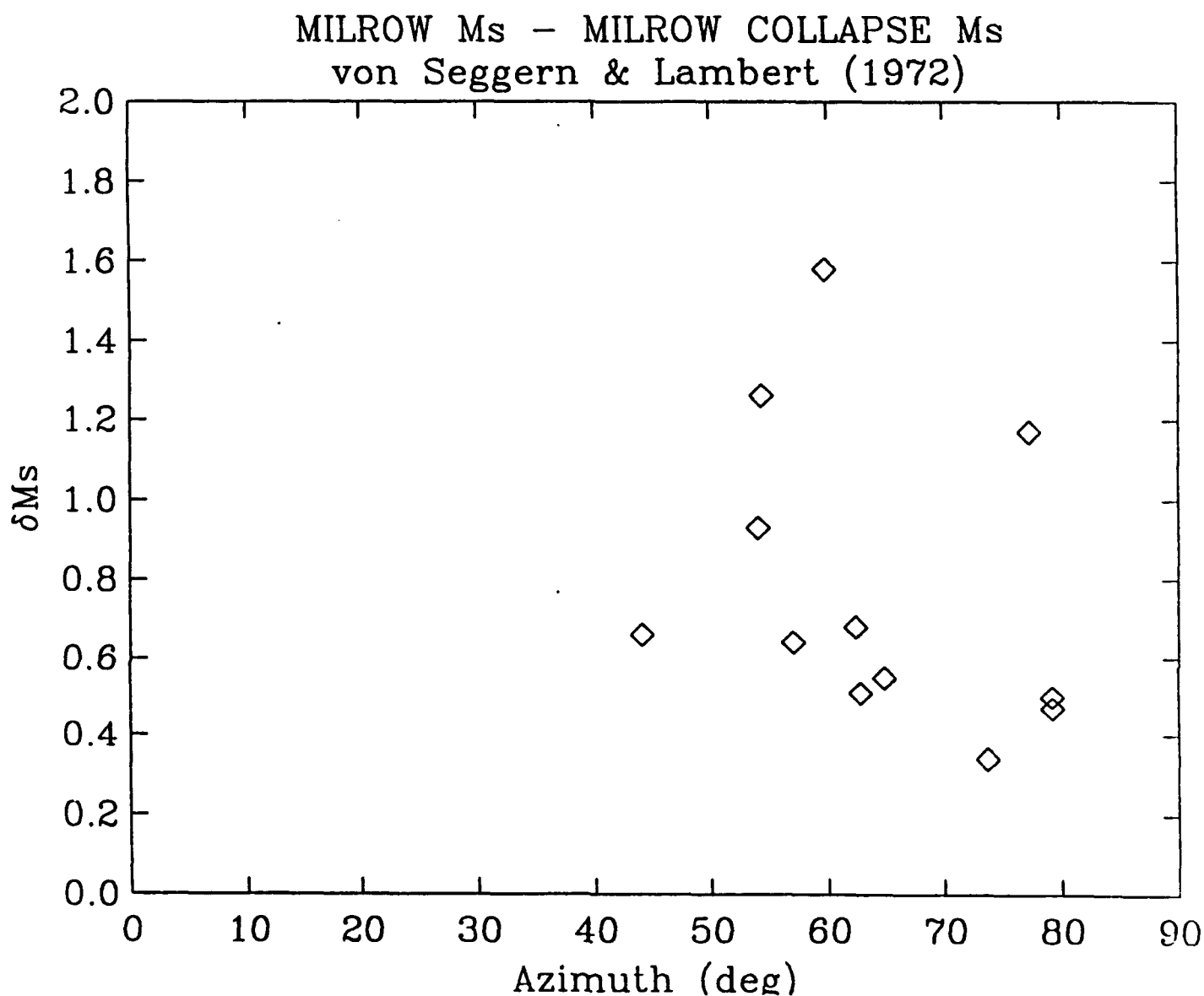
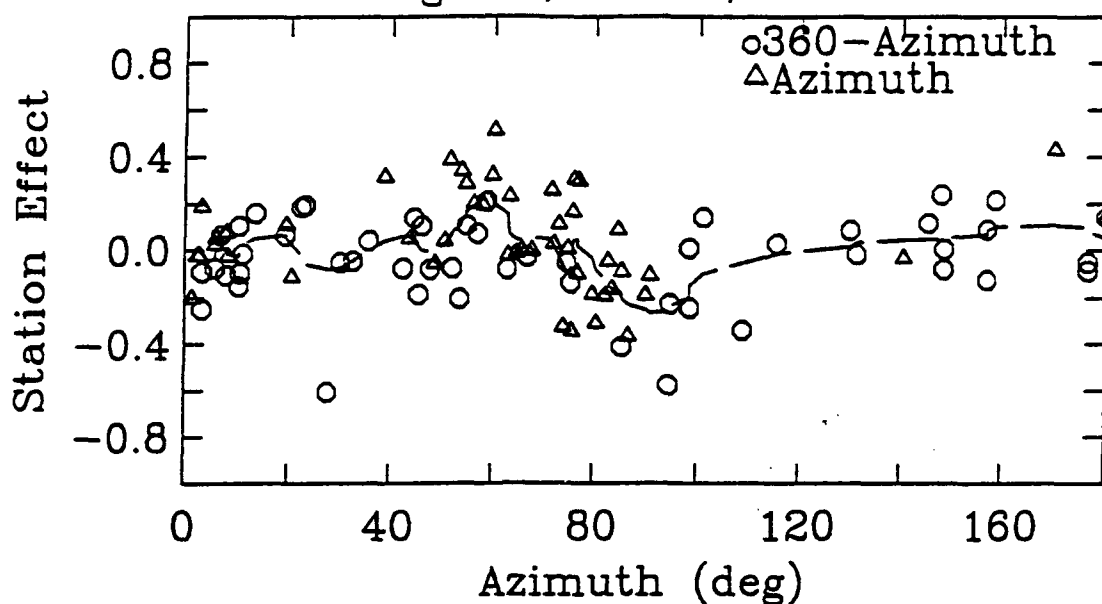


Figure 6. MILROW station explosion minus collapse Ms. There is no significant trend in the data between 40 and 90 degrees. If the collapse was an axisymmetric source then much of the amplitude pattern in Figure 5 is due to propagation effects and not tectonic release.

Maximum Likelihood WWSSN Ms Station Effects
Longshot, Milrow, Cannikin



Maximum Likelihood WWSSN Ms Station Effects
Longshot, Milrow, Cannikin

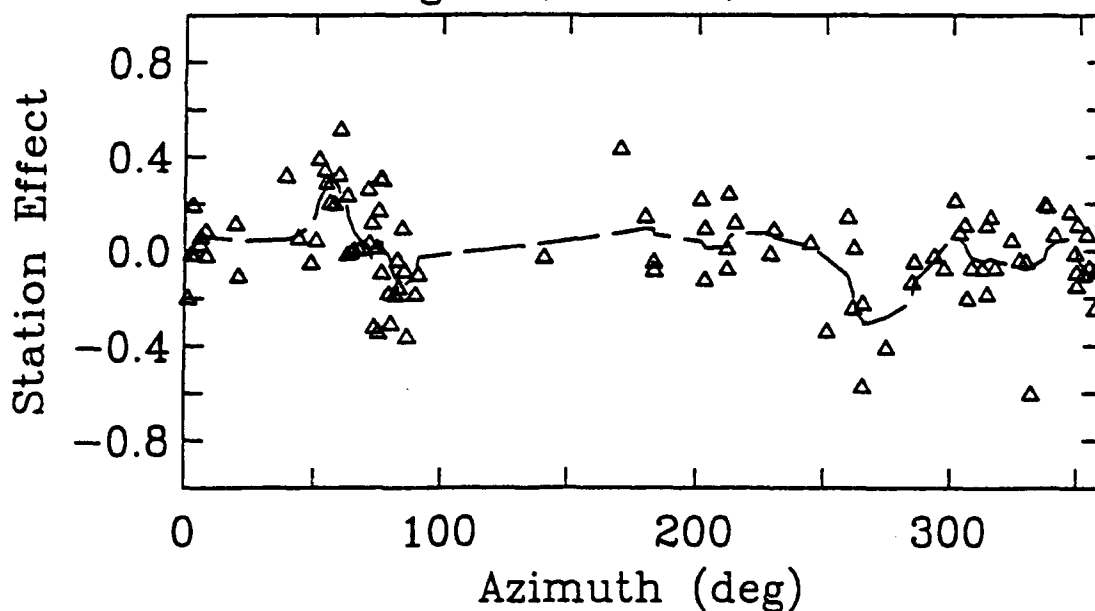


Figure 7. Maximum likelihood station effects for Ms magnitudes read at WWSSN stations from LONGSHOT, MILROW, and CANNIKIN. Station effects are plotted from 0 to 360 degrees (bottom) and from 0 to 180 degrees (top). The data appears to be consistent with a reflection symmetry about a north-south axis as would be suggested by the symmetry of the Aleutian subduction zone in the region of Amchitka. A nonparametric smoother has been applied to the data (dashed lines).

dominant source of Love waves. Both the analysis of Willis, *et al.* and that of von Seggern assumed that collapses are axisymmetric sources, yet these authors arrive at contradictory conclusions. Engdahl (1972) however, presents double-couple focal mechanisms for CANNIKIN collapse events that suggest normal faulting on 45 degree dipping planes striking roughly east-west. These focal mechanisms are based on locally recorded P-wave first motions. It is possible that these double-couple focal mechanisms do not reflect the actual long-period nature of the collapse; however, if the collapses are non-isotropic, then the simple ratio of the explosion-to-collapse does not represent the pure explosion plus double-couple radiation pattern. Further evidence that the local stress regime is influenced by the collapse is the observation that microearthquake activity around the explosion site undergoes an abrupt reduction immediately following the collapse. This behavior was observed for MILROW and CANNIKIN (Engdahl, 1972) and is common for events at NTS. Consequently, although the explosion-to-collapse amplitude ratios do cancel propagation and instrumental effects, it is not clear that they reveal a pristine source radiation pattern for all explosions. The resulting pattern may reflect the combined source radiation pattern of both the explosion and collapse. Therefore from the analyses of Willis, *et al.* and von Seggern it is clear that the explosions are contaminated by both tectonic release and path propagation effects but by an undetermined amount.

In addition to the presence of Love waves and the strong azimuthal radiation patterns from Amchitka explosions, it has been suggested that there was an apparent bias between Rayleigh wave excitation from Amchitka explosions and NTS explosions of similar size. von Seggern (1978) examined M_s for megaton NTS events compared to the M_s from MILROW and CANNIKIN. He concluded that M_s from the Amchitka events was low relative to the NTS events by as much as 0.5 magnitude units. M_s values determined by Marshall, *et al.* (1979) and moments determined by Stevens (1986b) and Stevens and McLaughlin (1989) suggest a bias closer to 0.2 log-units.

With propagation effects superimposed on the tectonic release radiation pattern, it is possible that this apparent bias is due to the nature of the network sampling afforded by the WWSSN, CSSN, and LRSM seismic networks that were used to estimate M_s and/or moment for these events. The networks are

heavily concentrated in North America and Europe where azimuthally dependent propagation could contribute to a bias in the estimation of the explosion part of the source. The most noticeable feature of this azimuthal pattern is the rapid decrease in Rayleigh wave amplitude with change in source-receiver azimuth between 40 and 70 degrees. This corresponds to high amplitudes for Canadian stations and low amplitudes for stations in southern North America. Coincidentally, this azimuthal range corresponds to ray-paths that propagate obliquely across the Aleutian subduction zone and are obliquely incident upon the North American continental margin. The observation that average WWSSN Ms station effects are consistent with a reflection about a north-south plane suggests that the near-source subduction zone striking east-west has introduced an apparent radiation pattern into the teleseismic Rayleigh waves.

In this study we examine the hypothesis that near-source 3D subduction structure has imposed an azimuthal pattern on the teleseismic Rayleigh wave amplitudes from the Amchitka test site. A 3D elastic finite difference code is used to simulate the propagation of long-period waves in a model of the Aleutian arc near Amchitka Island.

3. 3D FINITE DIFFERENCE METHODS

The use of 2D finite differences has become increasingly popular to simulate scalar (acoustic) and elastodynamic wavefields. As the speed and memory capacity of computers has increased, realistic seismological 3D finite difference calculations have become possible.

The principal advantage of 3D elastodynamic finite differences is that the calculations implicitly include all conversions and scattering. The principal disadvantage is that a limited bandwidth can be studied and the computer time is proportional to the fourth power of the size of the model and bandwidth. By limiting the bandwidth and model size, long-period near-source scattering presents a tractable problem that requires only a few compromises. However, by going to smaller models, the bandwidth of interest can be increased. For example, while our simulations explore 0.05 Hz waves in a model 800 km across, a model 40 km across could be used to explore 1.0 Hz waves with the same number of nodes. Although the simulations reported in this paper were performed on a CRAY-2 supercomputer using vector processing, problems of this size are within reach of many modern mini-supercomputers.

4. THE MODEL

We used a 3D explicitly time-stepping linear elastic finite difference method to calculate the response to an explosion source of a model for the Aleutian subduction zone in the region of Amchitka. Our objective was to accurately model elastic waves with periods 20 seconds or longer over a region extending 400 km from Amchitka island in all directions. To achieve this resolution and spatial extent efficiently, we generated a finite difference grid with an inner, finely gridded region with 6 km spacing. Outside this high-resolution inner grid, the spacing was slowly expanded at a constant rate of increase. In the region of expanding grid, artificial viscosity was increased to damp reflections from the expanding grid and the outer boundaries of the 3D grid. In this way, reflections from the outer edges are eliminated and do not contaminate the inner portion of the grid. In addition, we took advantage of a natural symmetry in the problem, assuming reflection symmetry about a north-south vertical plane passing through the source. The inner portion of the grid was 70x70x140 grid points (420 by 420 by 840 km). The time step was 0.25 sec. Figure 8 illustrates this use of an expanding, attenuating grid outside the inner grid. The total grid used in the computation was 100 by 100 by 200 or 2 million grid points. A 840 by 840 km box is superposed on top of a map of the Amchitka region in Figure 9. The P-wave velocity, S-wave velocity, density, and viscosity were specified at each grid point.

The velocity structure for the model was derived from two sources. Shallow structure for the area from marine seismic profiles was reviewed by Lambert, *et al.* (1970). They present a model with maximum crustal thickness between the island and the trench (about 40 km), and thinning crust behind the arc to merge with a normal oceanic crust. We chose the oceanic PREM model north and south of the subduction zone as the limiting far-field velocity model. The mantle velocity from the spherically symmetric PREM model (Dziewonski and Anderson, 1983) was perturbed in accordance with a thermal model for the subducting lithosphere from Boyd and Creager (1991). Boyd and Creager used local seismicity, P-wave residuals sphere analysis and travel times from the CANNIKIN explosion to constrain the geometry of the subducting Pacific plate under the Aleutian Islands. Their analysis was guided by a thermal model for the subducting slab. The study of Boyd and Creager follows a long line of

3-D Finite Difference Grid

Expanding and Attenuating Grid

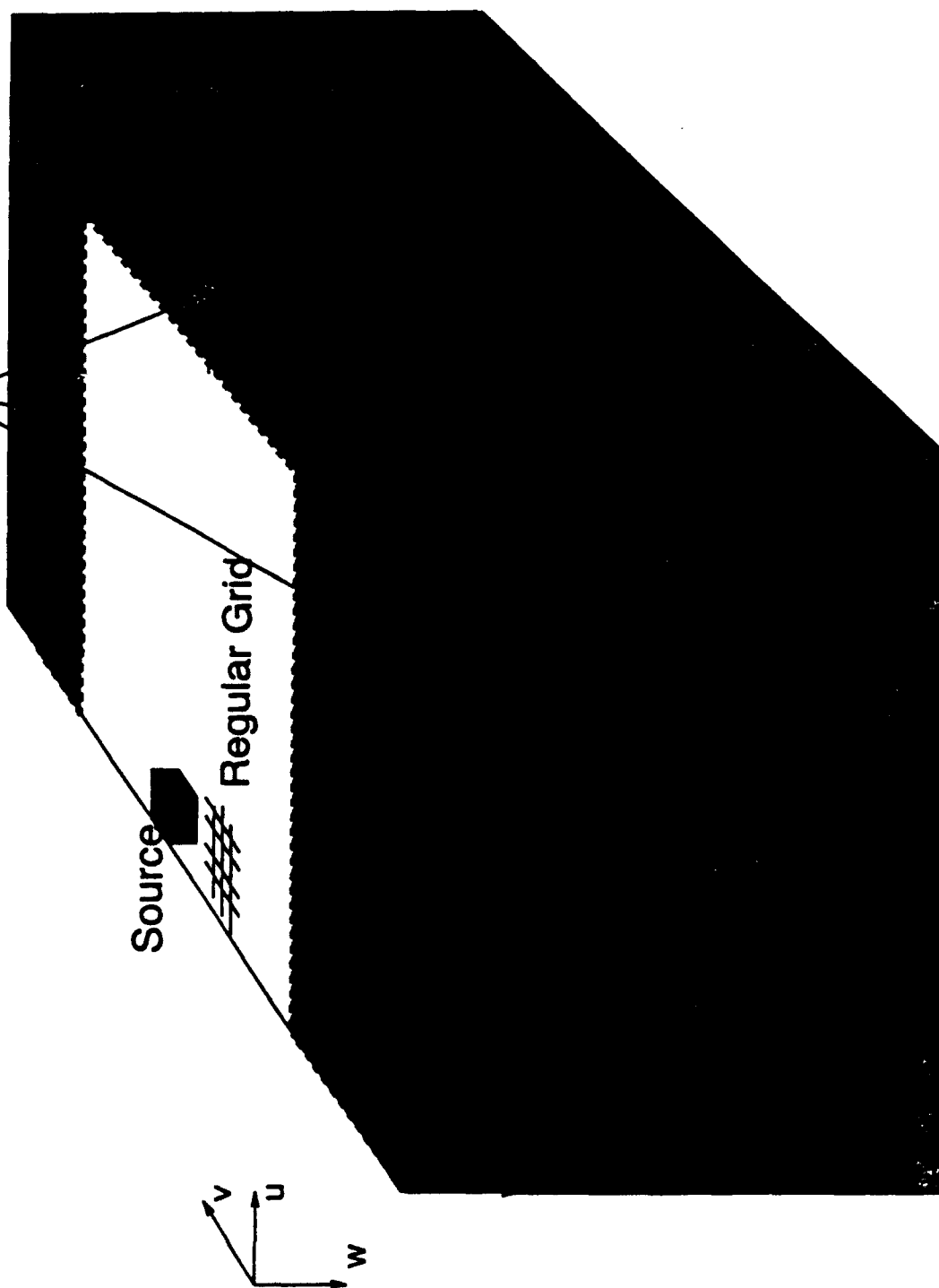


Figure 8.

The 3D finite difference grid was oriented with the v axis aligned north, u axis east and z axis down. A reflection symmetry boundary condition was used on the $u = 0$ plane taking advantage of the north-south reflection symmetry of the subduction zone. The inner grid had 6 km spacing and was $140 \times 70 \times 70$. The outer portion of the grid had a progressively expanding spacing. The entire grid was $200 \times 100 \times 100$. Numerical viscosity was used to damp reflections from the expanding grid. A 0.25 second time step was used.

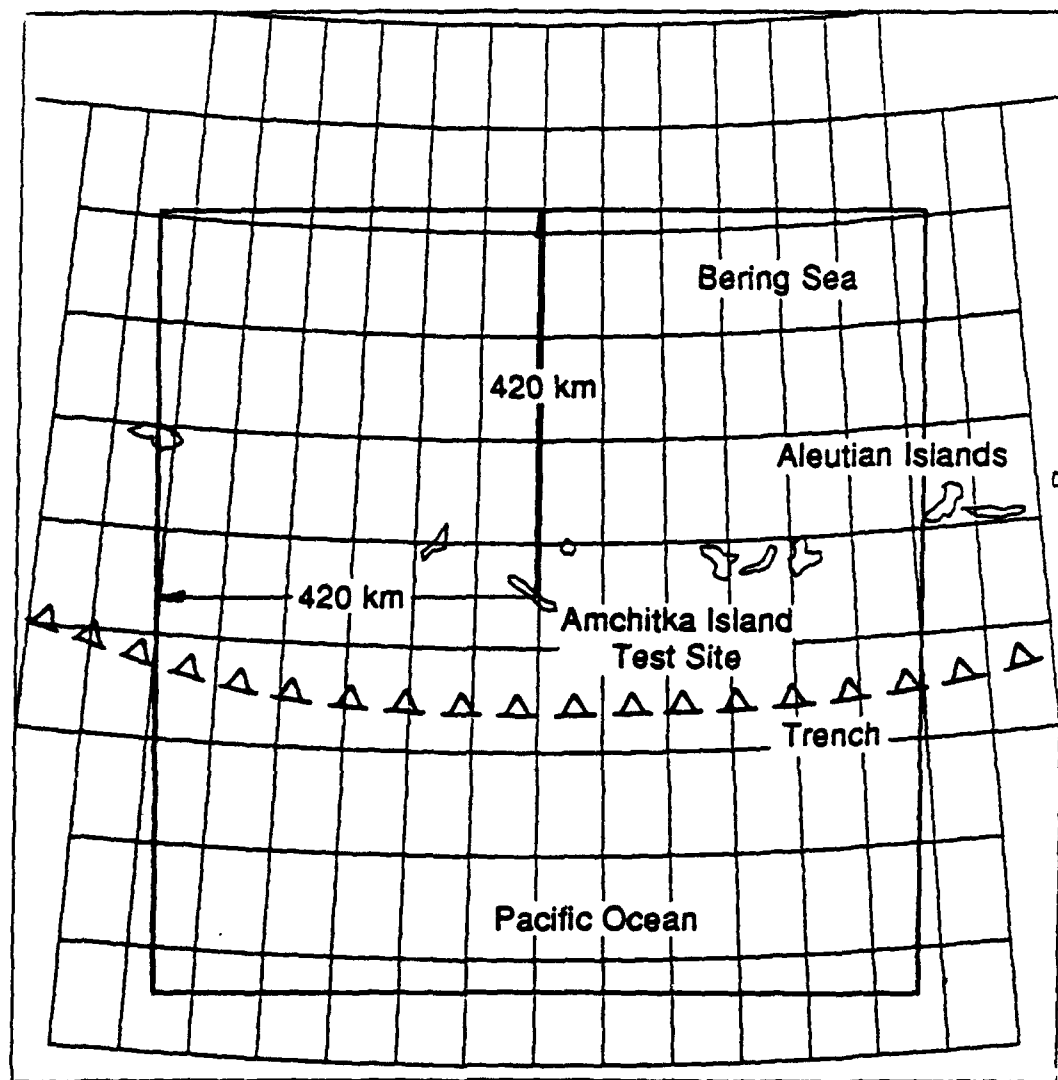


Figure 9. Map of region around Amchitka Island test site showing the approximate location of the trench axis and an 840 by 840 km box representing the finite difference grid used in the simulations.

studies that have examined teleseismic P-wave travel time anomalies from Amchitka Island explosions (for example see Chiburis and Ahner, 1969; Jacob, 1972; Page, 1972; Davies and Julian, 1972; Sleep, 1973; Cormier, 1990). P-wave and S-wave velocity contours are shown for the finite difference model in Figure 10.

The oceanic water layer was not included in the 3D calculations. The effect of the island/ocean interface was instead modeled in a separate series of 2D axisymmetric finite difference simulations (Stevens, *et al.*, 1990). The results of this study show that in cases where an island rises steeply out of the ocean, the Rayleigh waves excited by an explosion can be sharply reduced. However, for the specific case of Amchitka Island, the bathymetry is too gentle to cause any significant amplitude reduction; the effect of the ocean and island/ocean interface on 20-50 second Rayleigh waves is negligible.

Two 3D linear elastic finite difference calculations were performed. In the first calculation, curvature of the Aleutian arc was ignored and the source was at location #1 indicated in Figure 10. In the second calculation, curvature of the subduction zone structure was included and the source location is indicated by #2 in Figure 10. Locations #1 and #2 bracket the location of Amchitka Island in the subduction zone structure, with the first closest to the approximate position of the island. A comparison of the two calculations shows similarities in the azimuthal effects, but it is clear that the final results are sensitive to the location of the source in the model and some model details. Some aspects of the velocity model are poorly controlled, such as the detailed thickness of the crust and the low velocity accretion zone north of the trench. For this reason, results are best considered as indicative of the magnitude and qualitative character of the probable effects of the subduction zone upon wave propagation.

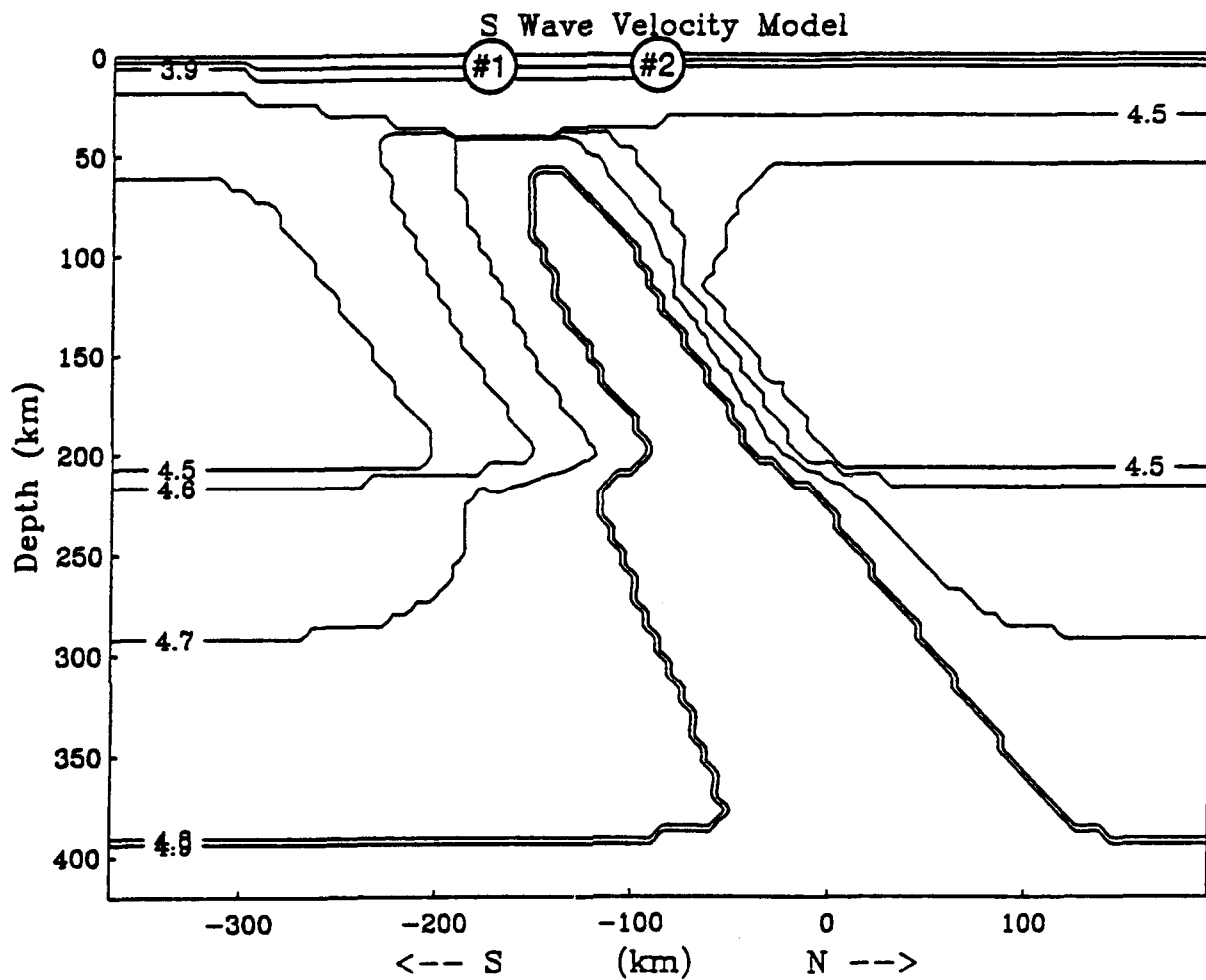


Figure 10. Contours of the S-wave velocity field along the north-south vertical plane. The model is based on Boyd and Creager (1991) and Lambert, *et al* (1970). Two simulations were conducted, with an explosive source at #1 and #2 indicated in the figure.

5. ANALYSIS AND DISCUSSION

Several analysis procedures were applied to the displacements on the surface of the grid. These included animated snap-shots of the displacement field at selected times, as well as procedures adapted from traditional surface wave data analysis, narrow band filter amplitude estimation, group and phase velocity estimation, and frequency-wavenumber analysis.

Animated snap-shots of the displacement field were resolved into vertical, radial, and transverse components in order to visualize the wave propagation. A color video of the evolving wavefield was made. The video movie was most helpful in visualizing the wave propagation and identifying areas for more detailed quantitative study.

Several monochrome (contour plot) snap-shots are shown in Figures 11A through 11D. The asymmetries in group velocity and amplitude are clearly evident from these figures. The structure to the east of the source along the strike of the structure is slower in the 20-30 second period range because of the low velocity sediments and thick crust along the trench axis. Consequently, there exists a narrow low-velocity zone that forms a channel for surface waves. Refraction around this channel causes focusing of surface wave amplitudes along the axis of the channel and defocusing in regions immediately off-axis (north and south) of the channel.

The snap-shots (Figure 11) of the transverse component of motion show a growing transverse wave that develops along the north and south margins of the low velocity channel. The transverse amplitudes are about 1/4 the amplitude of the radial Rayleigh wave and appear to be associated with the passage of the Rayleigh wave along the edges of the low-velocity channel. Frequency-wavenumber spectra were used to confirm the presence of Love wave type motion.

Arrays of grid points were selected at locations on the surface of the grid and frequency-wavenumber (FK) spectra were estimated from the three components of motion. Figures 12 and 13 show FK spectra from synthetic arrays at azimuths of 68 and 160 degrees respectively. Array #1 at an azimuth

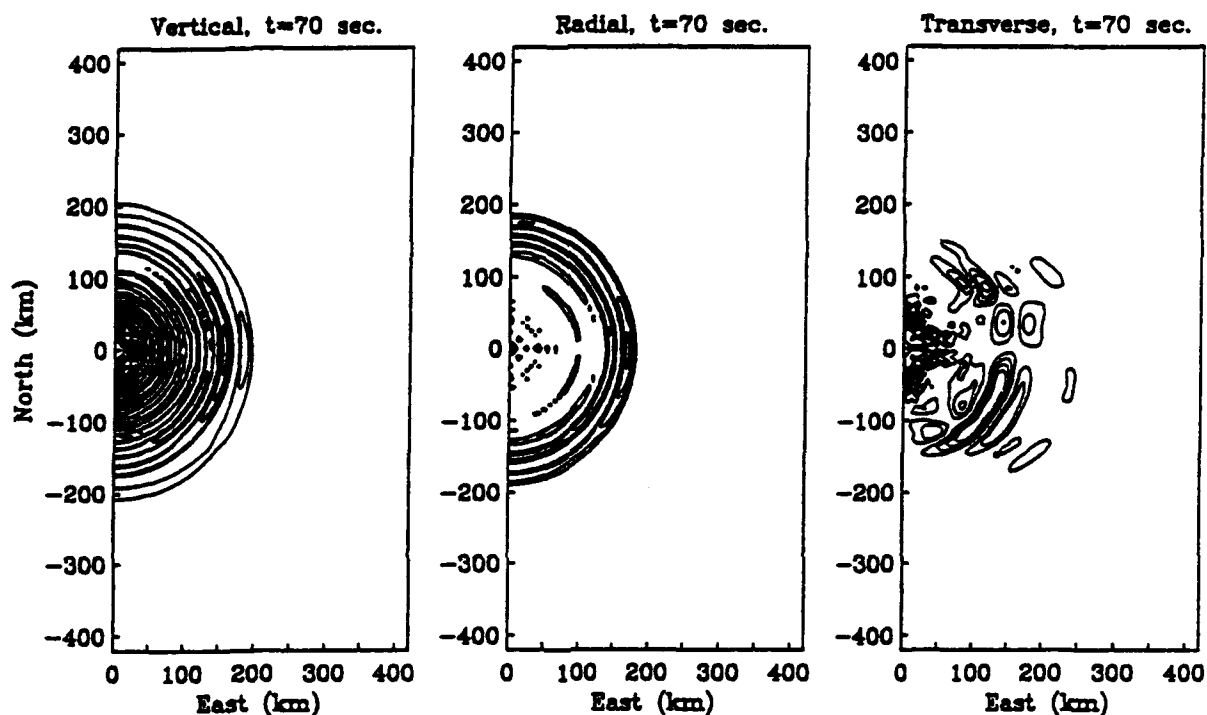


Figure 11A. Contours of displacement amplitude of the vertical, radial, and transverse components of motion on the free-surface of the finite difference grid at time $t = 70$ seconds. The motion is dominated by the fundamental Rayleigh wave on the vertical and radial components. Note the transverse motion beginning to form behind the Rayleigh wave southeast and northeast of the source. Simulation 3D#1.

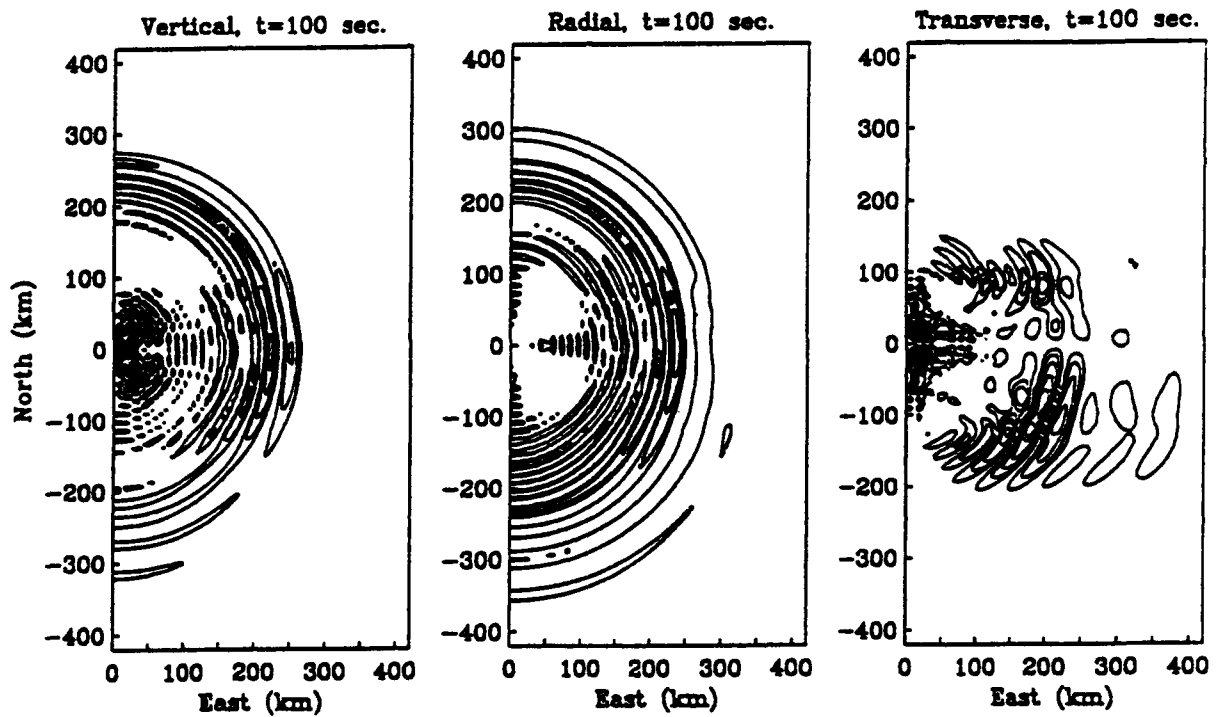


Figure 11B. Contours of displacement amplitude of the vertical, radial, and transverse components of motion on the free-surface of the finite difference grid at time $t = 100$ seconds. Asymmetry in the Rayleigh wave amplitude and arrival time can be seen in the vertical and radial components. Note the transverse Love wave motion behind the Rayleigh wave southeast and northeast of the source. Simulation 3D#1.

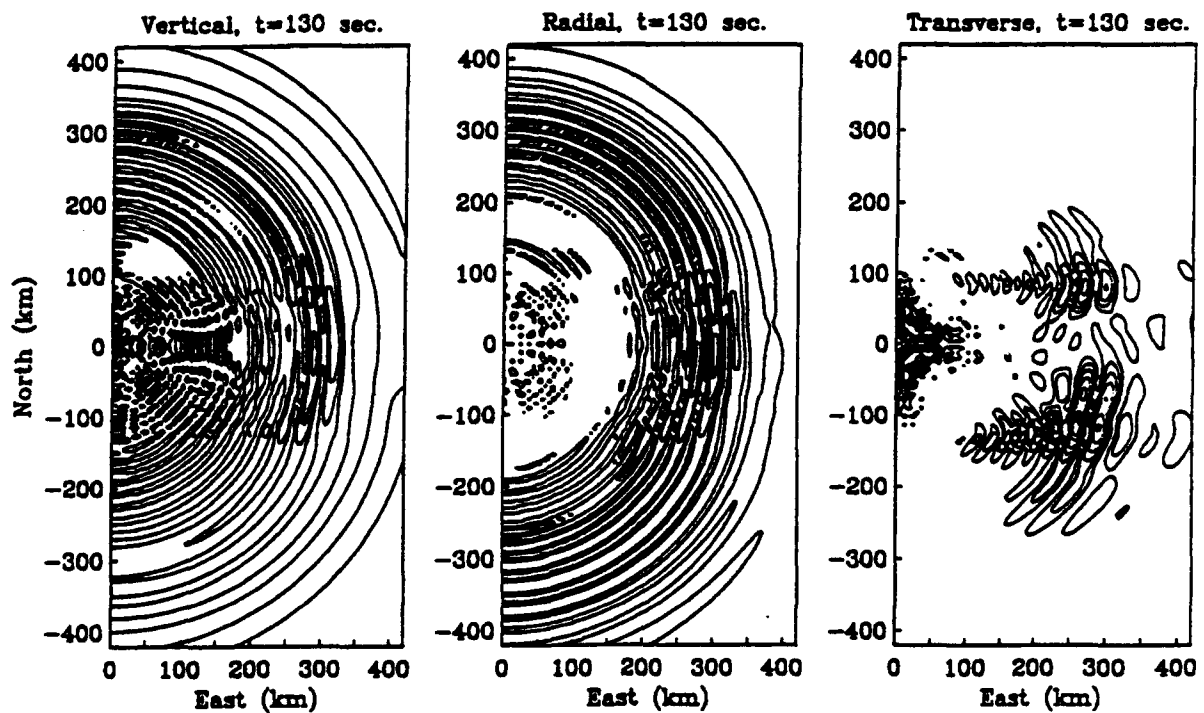


Figure 11C. Contours of displacement amplitude of the vertical, radial, and transverse components of motion on the free-surface of the finite difference grid at time $t = 130$ seconds. Rayleigh wave motion is both stronger and delayed to the east along the axis of the subduction zone. Love wave motion southeast and northeast of the source is beginning to overtake the Rayleigh wave motion. Simulation 3D#1.

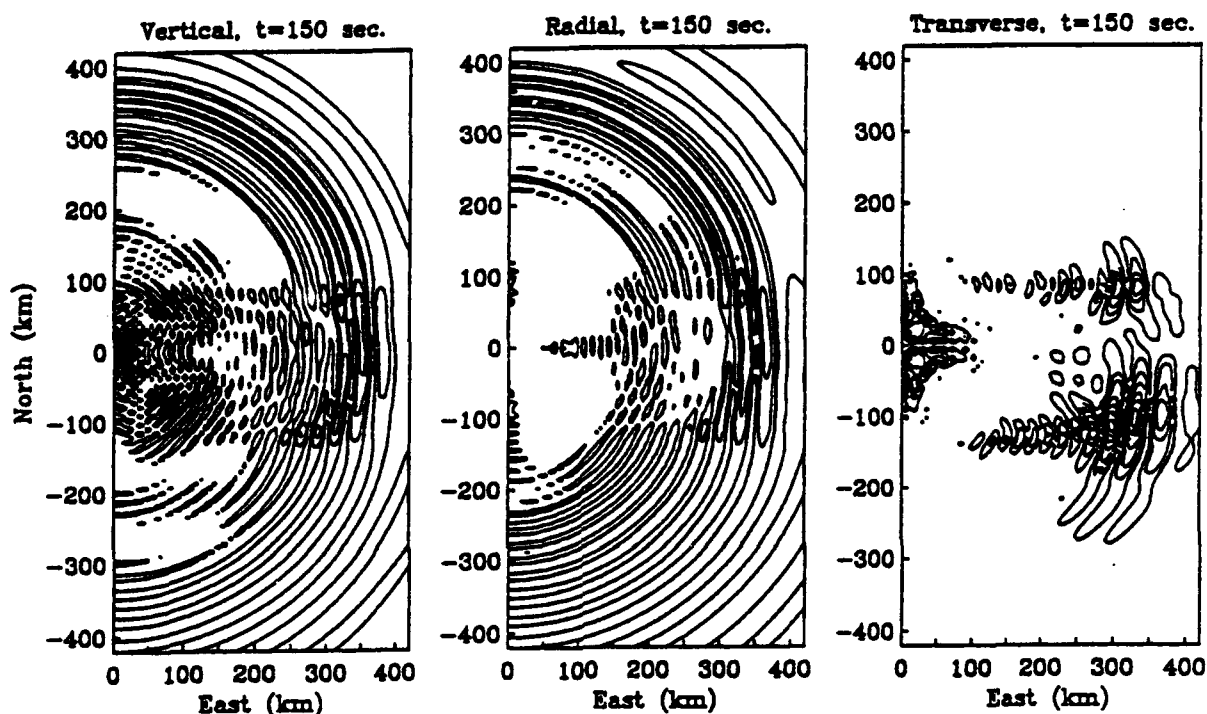


Figure 11D. Contours of displacement amplitude of the vertical, radial, and transverse components of motion on the free-surface of the finite difference grid at time $t = 150$ seconds. Rayleigh wave motion is both stronger and delayed to the east along the axis of the subduction zone. Love wave motion southeast and northeast of the source is overtaking the Rayleigh wave motion. Simulation 3D#1.

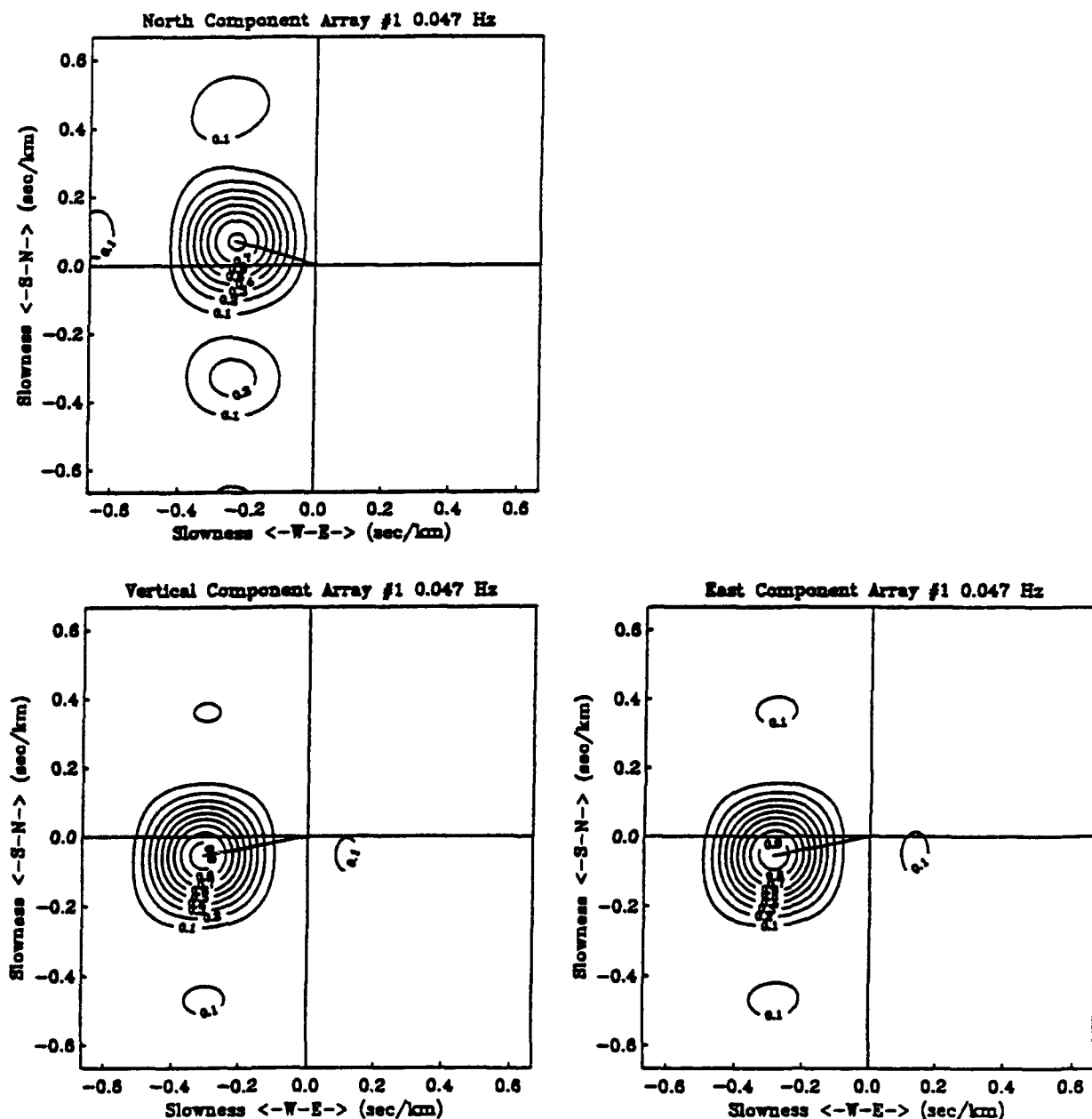


Figure 12. Wavenumber spectra at 0.047 Hz from a synthetic array of stations located 300 km from the source at an azimuth of 68 degrees. The vertical and east components show a prominent arrival with a phase velocity of about 3.3 km/sec propagating at an azimuth of 80 degrees. The north component shows an arrival propagating at 4.0 km/sec and 107 degrees. The vertical and east component see a 12 degree off azimuth Rayleigh wave while the north component records a 40 degrees off azimuth Love wave.

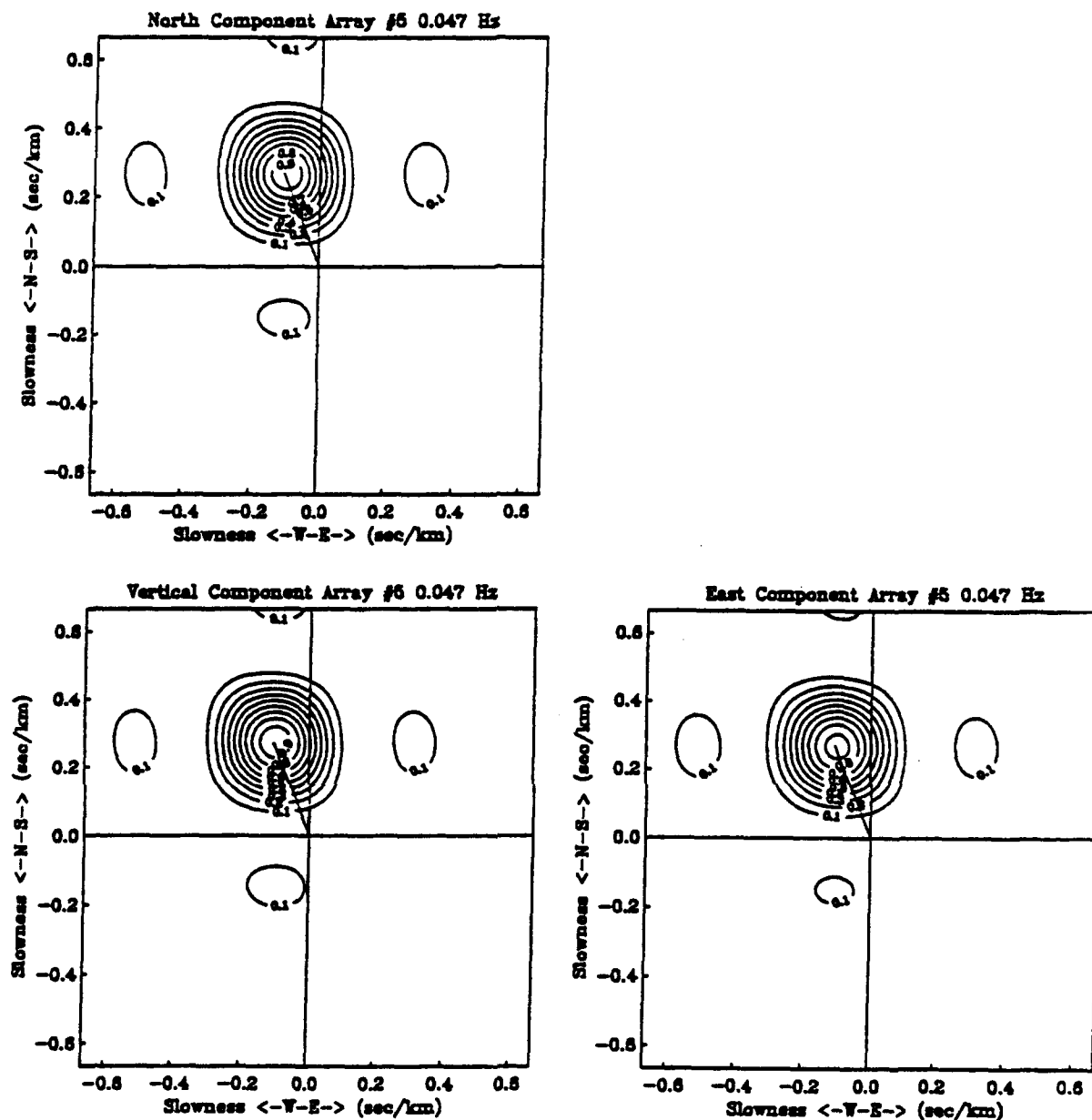


Figure 13. Wavenumber spectra at 0.047 Hz from a synthetic array of stations located 300 km from the source at an azimuth of 160 degrees. All three components show a prominent arrival with a phase velocity of 3.44 km/sec propagating at an azimuth of 158 degrees. The Rayleigh wave is on azimuth from the source.

of 68 degrees shows a prominent arrival propagating with a phase velocity of 3.2-3.4 km/sec at an azimuth of 80 degrees on the vertical and east components. The north component shows a prominent arrival propagating with a phase velocity of 4.0 km/sec at an azimuth of 107 degrees. The FK spectra demonstrate that the transverse component waves (north) propagated at Love wave phase velocities but in a direction 40 degrees from the source to receiver azimuth. All three components of FK spectra demonstrate that both the Rayleigh and Love wave fields are refracted along the low-velocity channel associated with the thick crust and low velocity accretionary wedge. Array #2 located at an azimuth of 160 degrees from the source shows all three components dominated by a Rayleigh wave propagating at a phase velocity of 3.44 km/s and an azimuth of 158 degrees. No Love waves are seen in the direction of array #2, and the Rayleigh wave is on azimuth.

In order to quantify the amplitude and velocity anomalies associated with the 3D wave propagation, conventional narrow bandpass filtering was used to examine the seismograms available across the free-surface of the grid. Figure 14A shows the vertical component traces for a distance of 270 km from the source. The traces are shown from 0 to 180 degrees azimuth. Note the larger amplitudes and delayed waveforms to the east. Similar effects are seen on the radial components, shown in Figure 14B at the same scale as the vertical components. The transverse components of motion are displayed in Figure 14C at a larger scale (5X) than the vertical/radial traces. The transverse components are largest in the 60-80 and 100-130 degree azimuth ranges.

Figure 15 shows the peak bandpass filtered Rayleigh-wave amplitudes as a function of azimuth for two frequencies and both simulations. Note that the large amplitudes tend to occur at the easterly azimuths but that the pattern is quite different for the two source locations (3D#1 and 3D#2). Figure 16 shows the peak Rayleigh-wave amplitudes as a function of azimuth for a fixed distance of 350 km compared to the arrival time. Note that the larger amplitudes tend to arrive late. Higher amplitudes tend to occur in slower directions. This analysis supports the contention that the low velocity region along the subduction zone focuses the surface wave energy. Because the sources are offset from the center of the wedge/trench axis the patterns are not symmetrical about the east-west azimuth.

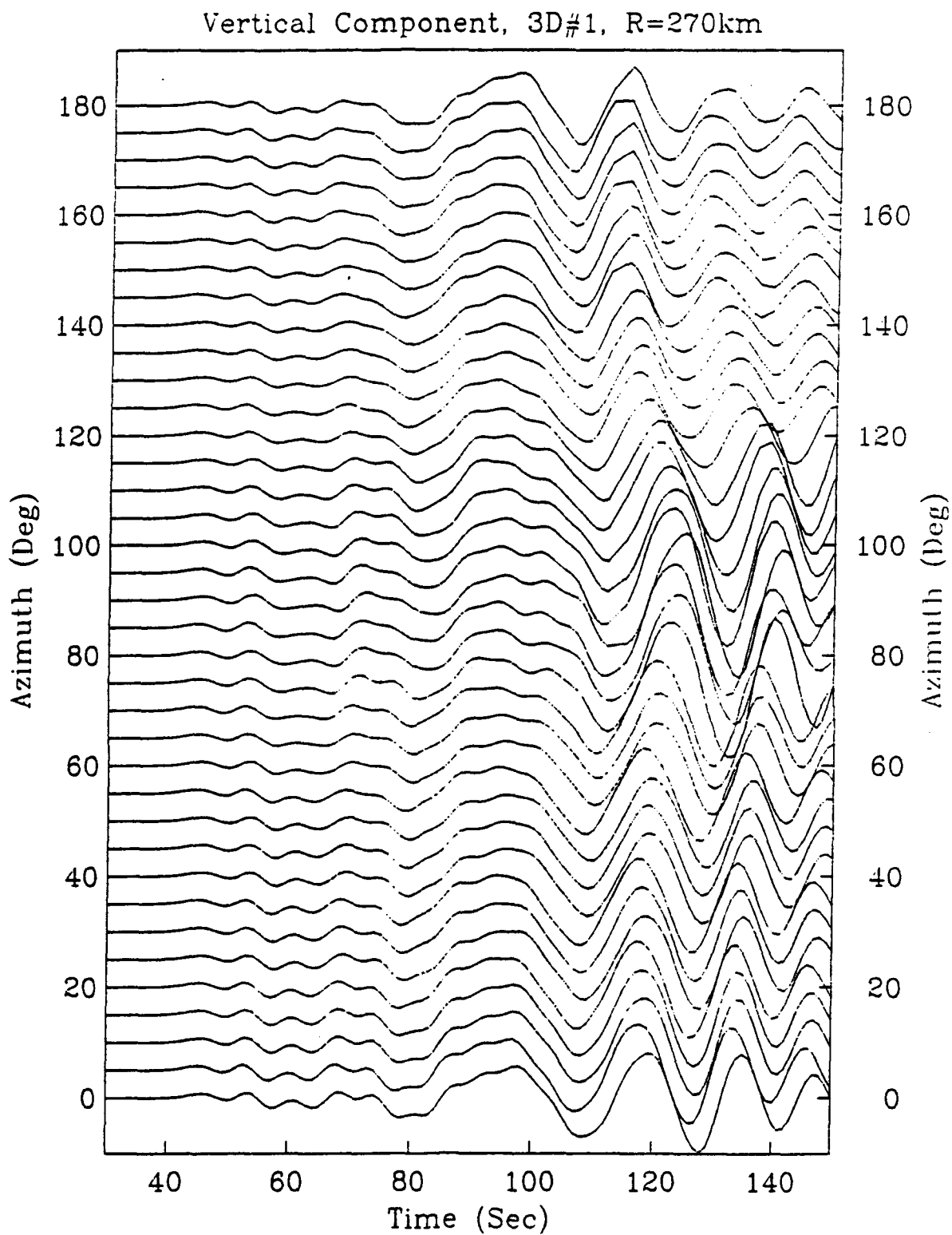


Figure 14A. Vertical component of motion displayed for a constant distance from the source, 270 km, as a function of time and azimuth. Note that the traces are delayed and larger amplitude to the east.

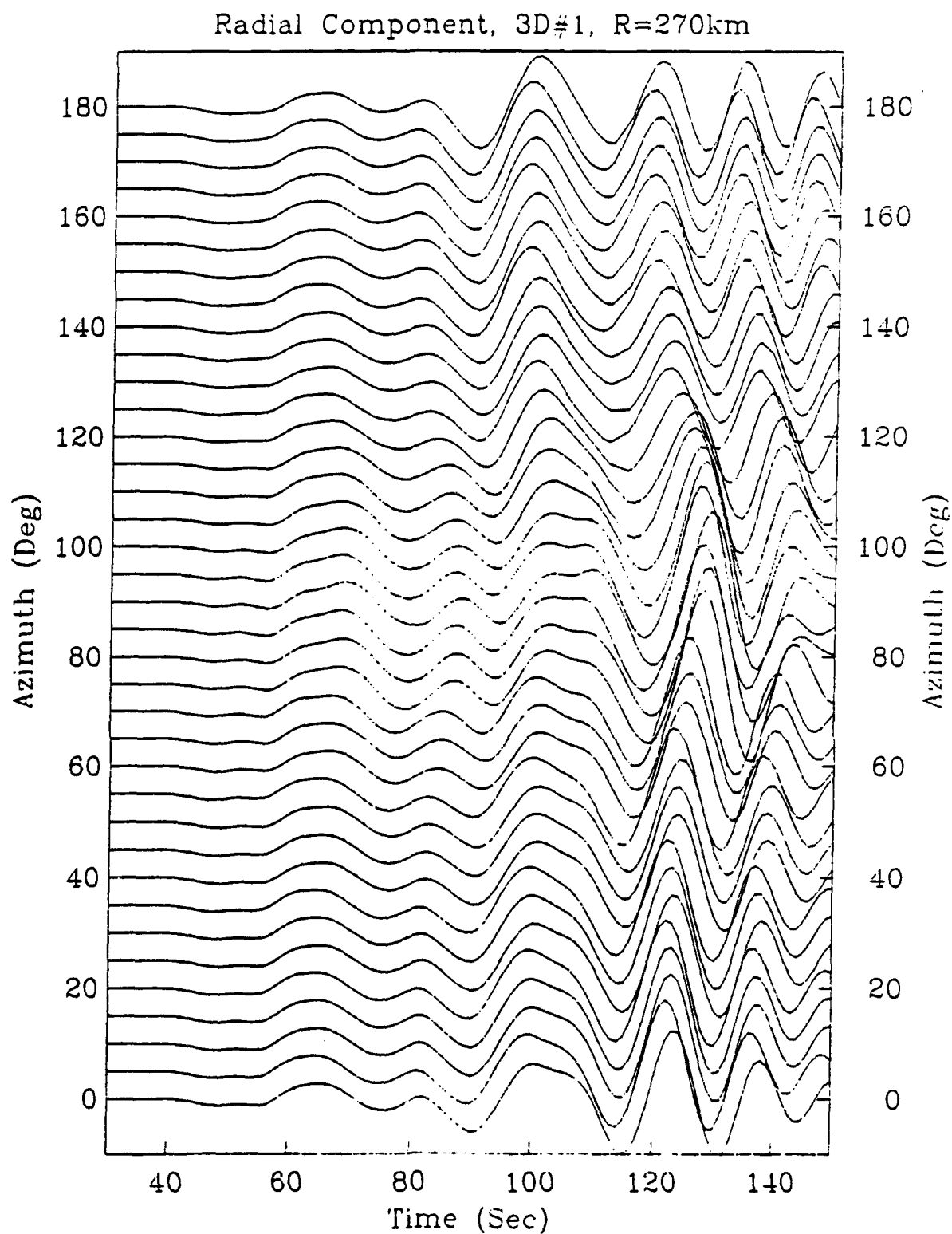


Figure 14B. Radial component of motion displayed for a constant distance from the source, 270 km, as a function of time and azimuth, same scale as vertical components. Note that the traces are delayed and larger amplitude to the east.

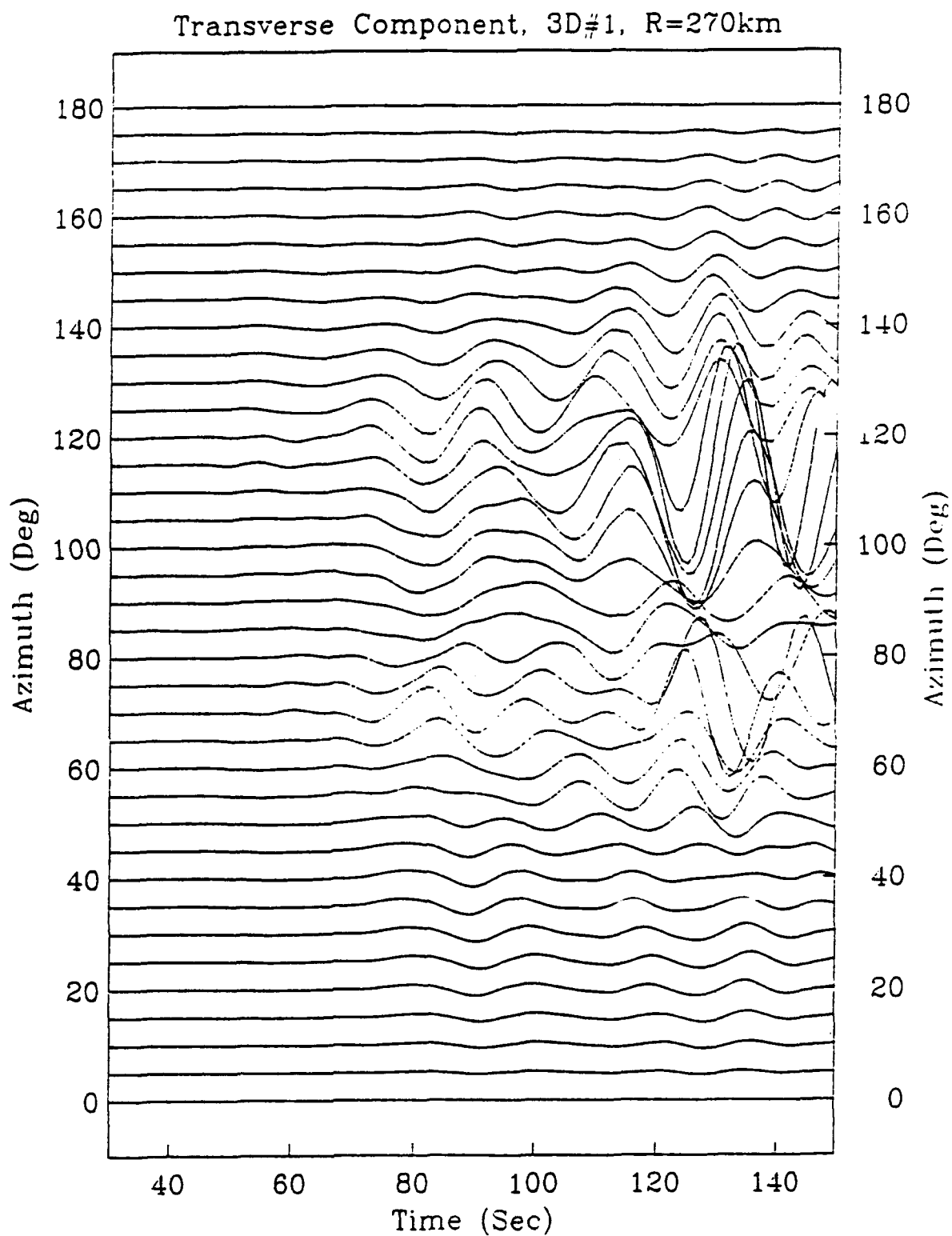


Figure 14C. Transverse component of motion displayed for a constant distance from the source, 270 km, as a function of time and azimuth, 5X scale as vertical/radial components. Note that the amplitudes are largest in narrow azimuthal ranges, 60-80 and 100-130 degrees.

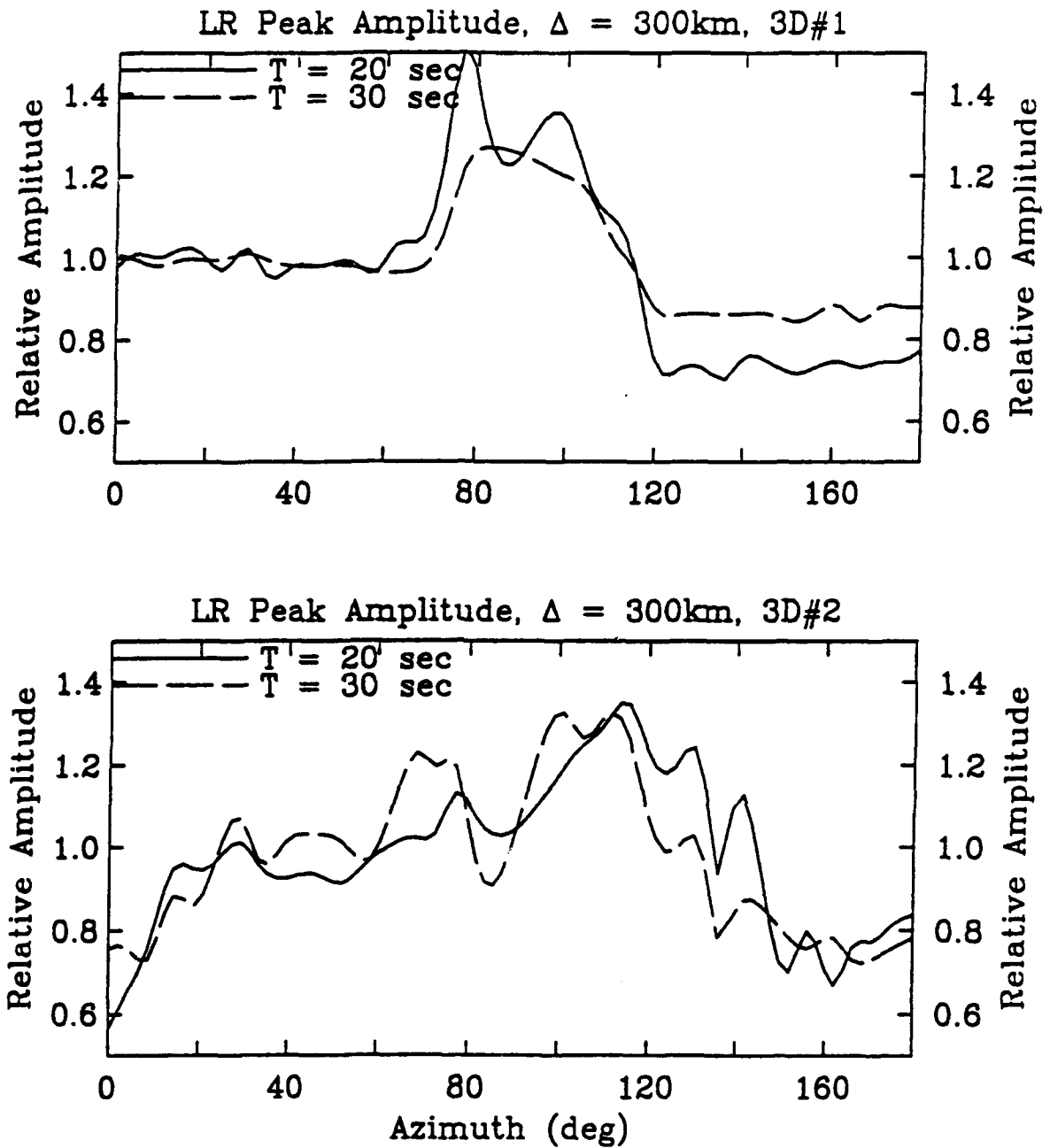


Figure 15. Peak bandpass filtered Rayleigh wave (LR) amplitude (periods of 20 and 30 sec) as a function of azimuth at a distance of 300 km from the source. Simulations 3D#1 and 3D#2 show similar patterns but significant differences in details of the patterns. Both simulations show factors of 2 in azimuthal variation at 300 km from the source.

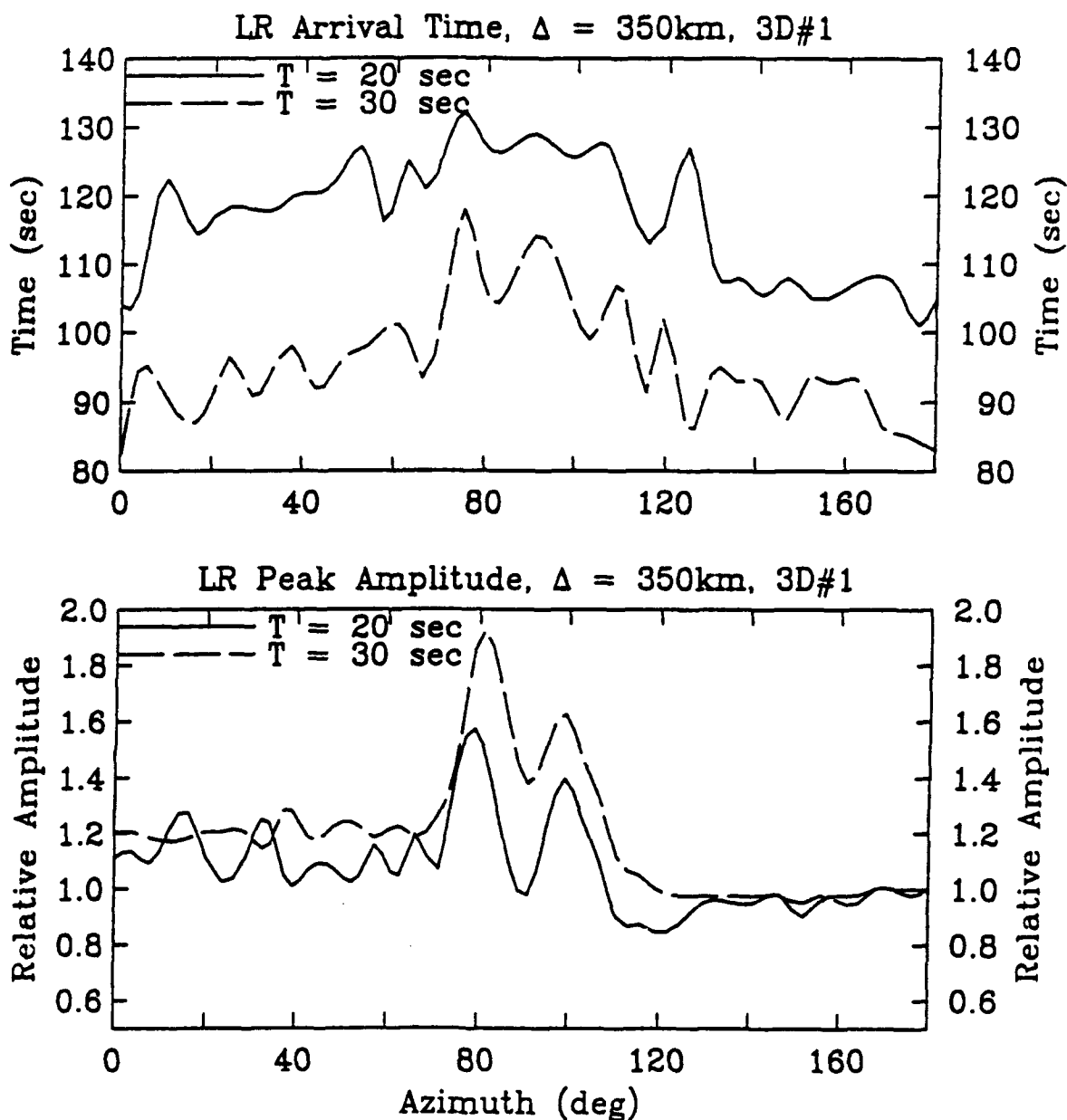


Figure 16. Peak 20 and 30 second Rayleigh wave amplitude at 350 km from the source (bottom) and the arrival time (top) for simulation 3D#1. Note the correlation between the arrival time and the amplitude. Amplitudes tend to be higher in slower directions. Focusing occurs along the trench axis 70-100 degrees.

In order to show the details of the surface wave amplitude anomalies across the surface of the grid, each vertical seismogram on the grid surface was narrow band filtered and the Rayleigh wave amplitude was estimated. Examples of these amplitudes are contoured in Figures 17A and 18A. The Amplitude contours show the effects of both normal geometric attenuation and azimuthal variation from the 3D propagation. Figures 17B and 18B show the amplitude contours corrected for $1/\sqrt{R}$ geometrical spreading. Due to near-field terms, the corrected amplitudes would not be constant even in the absence of lateral heterogeneity, but the $1/\sqrt{R}$ correction does serve to bring out the azimuthal anomalies and the fact that the anomalies tend to grow with distance as the focusing/defocusing lateral refraction progressively disturbs the wave field.

To compute Rayleigh amplitudes at teleseismic distances, we developed a Fresnel-Kirchoff integral procedure to propagate surface waves to teleseismic distances and account for diffraction of the wavefront. A derivation of the application of Fresnel-Kirchoff diffraction theory to surface waves is contained in Appendix I. This method assumes that the surface waves propagate from the edge of the 3D grid into a laterally homogeneous earth structure to receivers far away without additional complication. This assumption allows us to calculate the effects of far-field diffraction from the near-source scattering modeled by the 3D finite difference grid.

To apply the Fresnel-Kirchoff integral we save the synthetic free-surface displacement seismograms, $u(r', t)$, on a circle of constant radius, R , from the source and apply the frequency-domain integral,

$$\hat{u}(r, \omega) = \frac{k}{2\pi} \int_0^{2\pi} \hat{u}(r', \omega) \frac{e^{ik|r-r'|}}{\sqrt{|r-r'|}} (\cos(\theta') + 1) R d\theta' \quad (9)$$

where $\theta' = \theta - \theta_0$ is the angle between the far-field receiver and the seismogram location.

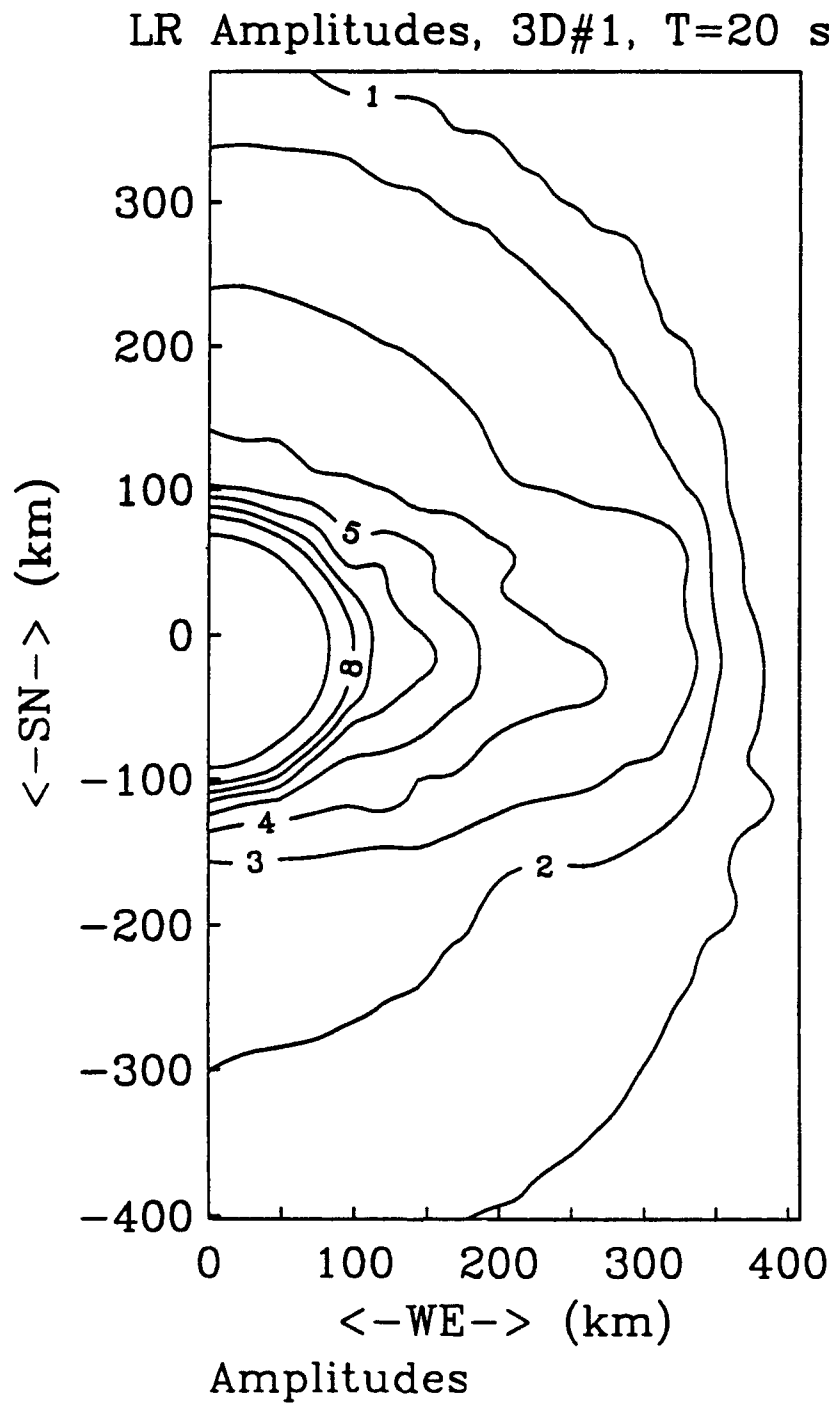


Figure 17A. Contours of peak LR amplitude at 0.05 Hz from simulation 3D#1. Note the elongation of the contours in the east west direction.

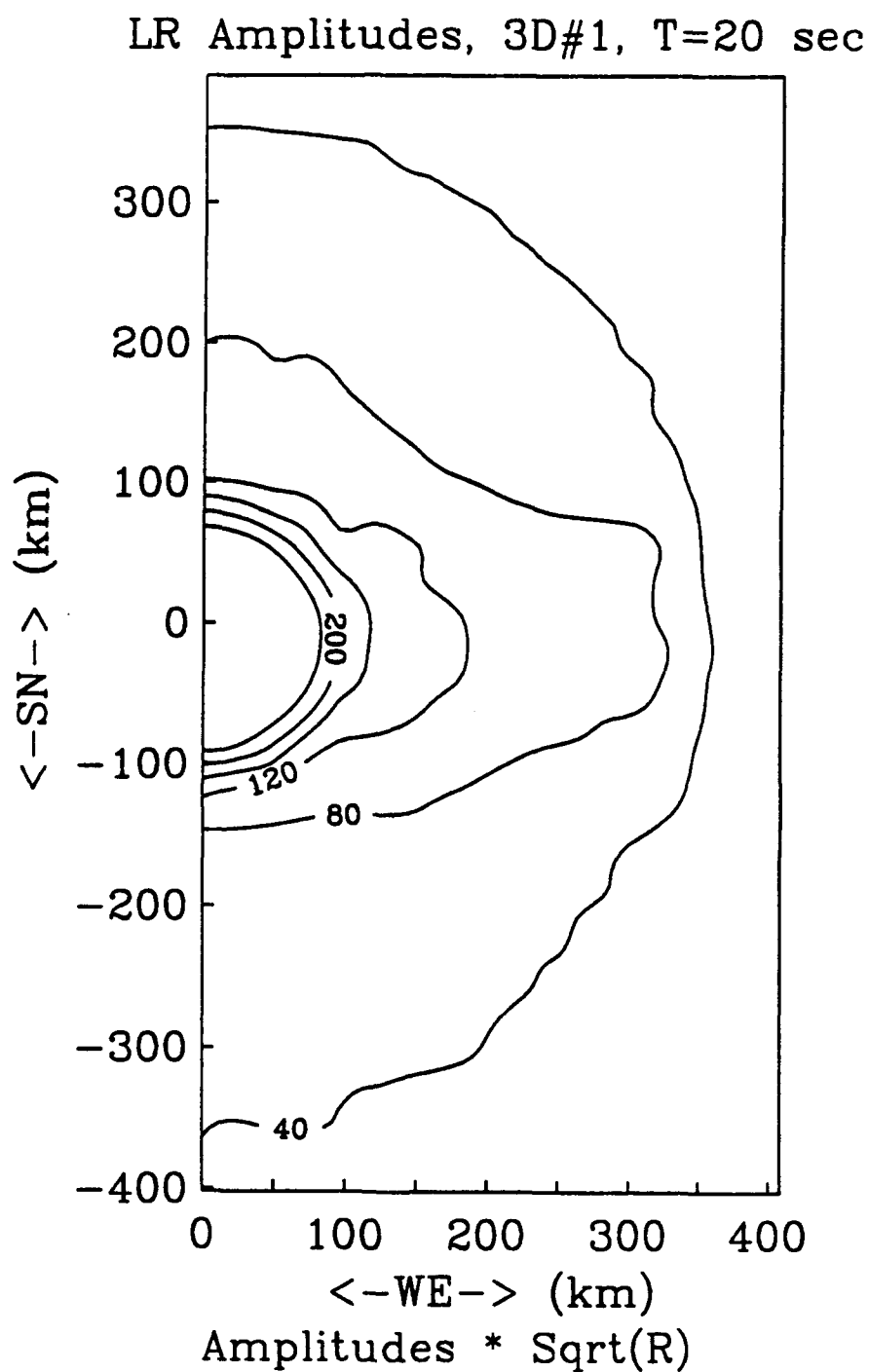


Figure 17B. Contours of peak LR amplitude at 0.05 Hz from 3D simulation 3D#1, corrected for $1/\sqrt{R}$ geometrical spreading. Note the elongation of the contours in the east west direction.

LR Amplitudes, 3D#2, T=20 sec

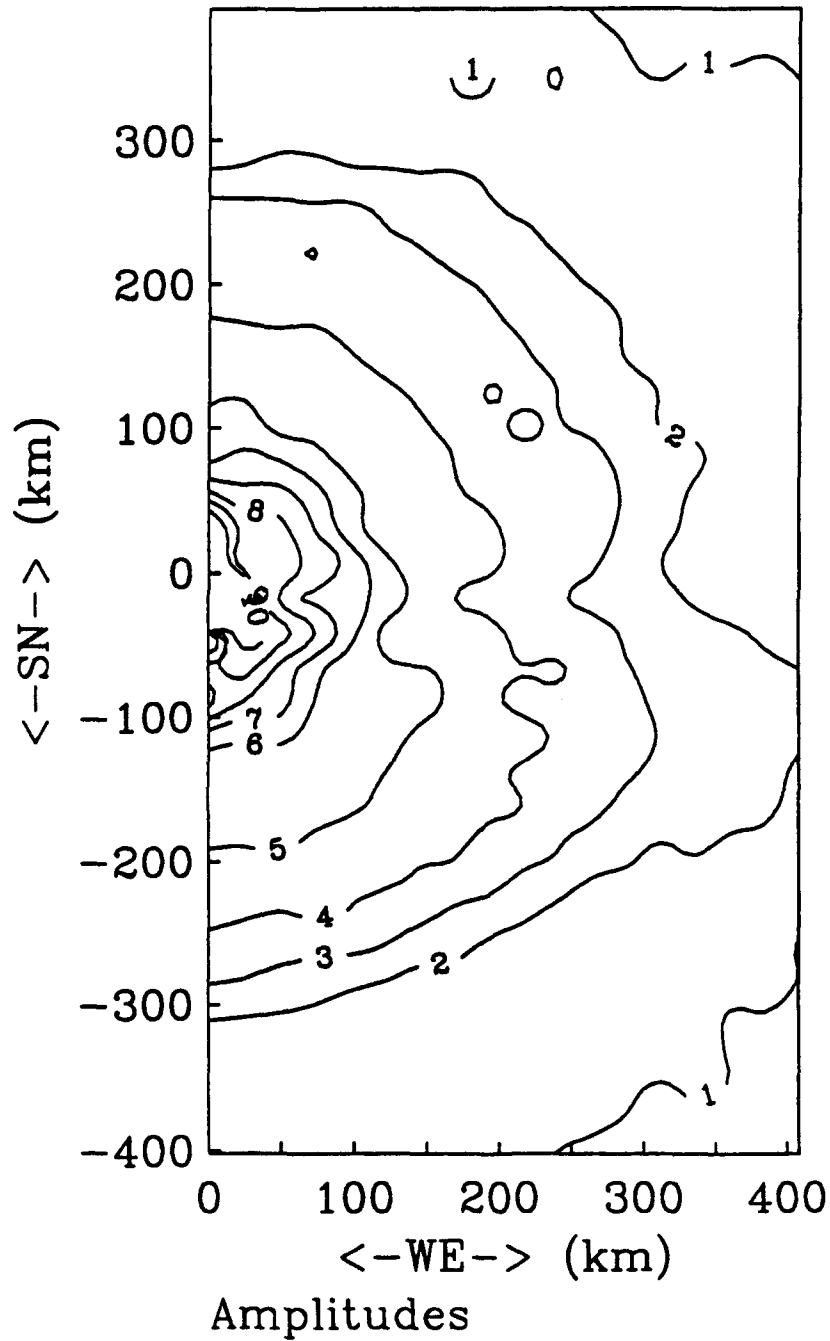


Figure 18A. Contours of peak LR amplitude at 0.05 Hz from simulation 3D#2. Note the elongation of the contours in the east west direction.

LR Amplitudes, 3D#2, T=20 sec

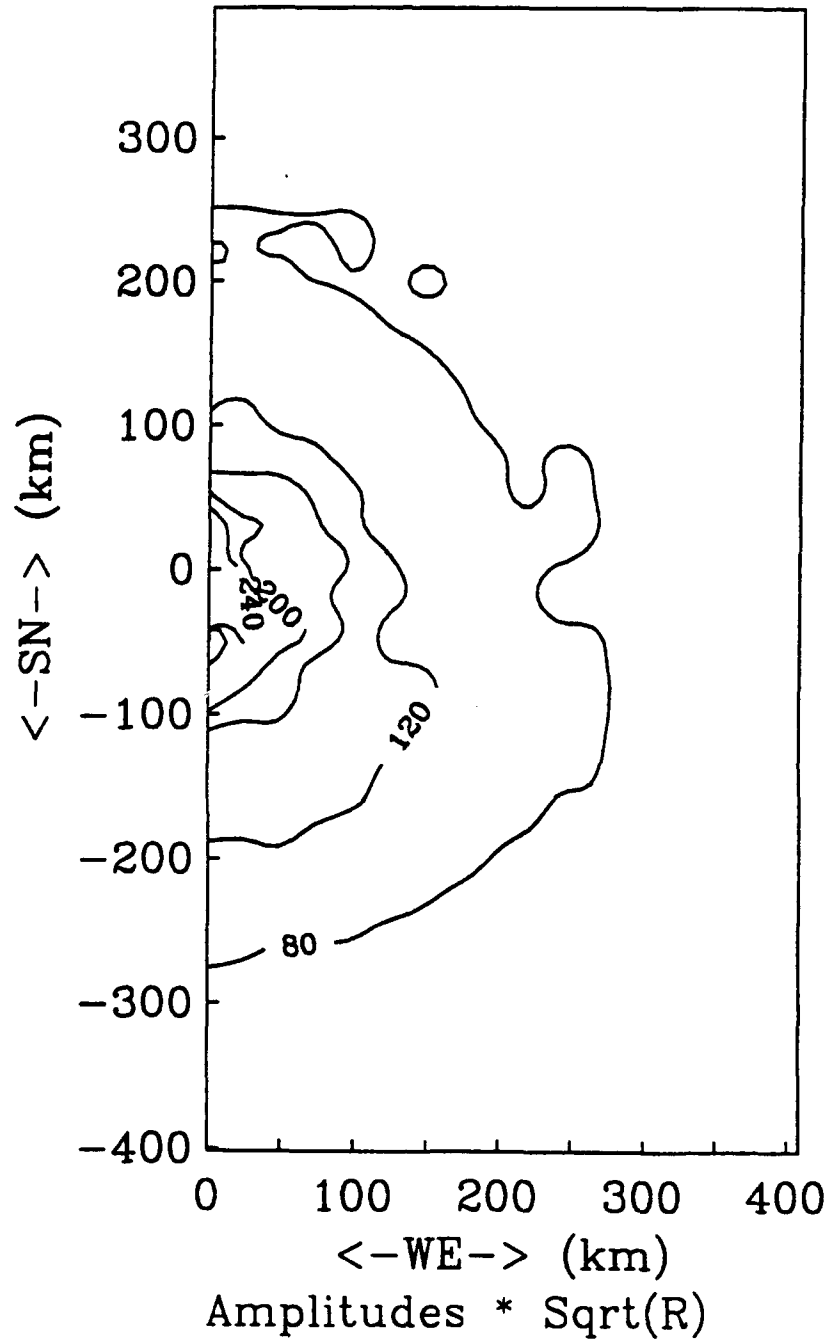


Figure 18B. Contours of peak LR amplitude at 0.05 Hz from simulation 3D#2, corrected for $1/\sqrt{R}$ geometrical spreading. Note the elongation of the contours in the east west direction.

The amplitude and phase of the free-surface seismograms at fixed distances from the source are plotted in Figures 19A and 19B for the two simulations. This information is utilized in the numerical integral to compute the far-field teleseismic surface wave amplitudes. The phase (delay-advance) of the wavefield as a function of azimuth at the integration distance, R , is just as important as the amplitude dependence in the final amplitude at the far-field receiver.

Note the negative correlation between amplitude and phase for simulation 3D#1 in Figure 19A. This suggests that focusing/defocusing is largely responsible for the amplitude pattern at this distance from the source. Note also that for both simulations the amplitude patterns are similar at different frequencies while the detailed patterns are frequency dependent. Figures 20A and 20B plot the far-field relative amplitude as a function of amplitude and frequency. Although the patterns are frequency dependent, the different frequencies share some common patterns. The average relative pattern from 32 to 20 seconds period is shown in the upper frame of Figures 20 A and B.

The dominant pattern of the observed amplitudes was high amplitudes in the northeast and low amplitudes to the east (Figures 1- 7). Neither simulation, 3D#1 or 3D#2, reproduces the exact observed pattern, but both simulations show focusing/defocusing patterns that have characteristics similar to the observed amplitude/magnitude patterns. The principal characteristic that both data and simulation exhibit is azimuth ranges of low amplitude adjacent to azimuth ranges of high amplitude. Both the data and the simulated amplitude patterns show azimuthally dependent variations that can exceed factors of 2 peak-to-peak over a broad frequency range. The amplitude patterns can be very narrow (10 or 20 degrees), uncharacteristic of the broad amplitude patterns from tectonic release which have amplitude perturbations proportional to $\sin(2(\theta - \theta'))$.

Although the hybrid finite-difference Fresnel-Kirchoff synthetic amplitude patterns do not reproduce the observed amplitude patterns it is clear that they do predict variations comparable to those observed. Furthermore, the two simulations, 3D#1 and 3D#2, illustrate that changes in the location of the source comparable to a wavelength (32 seconds) alter the amplitude pattern

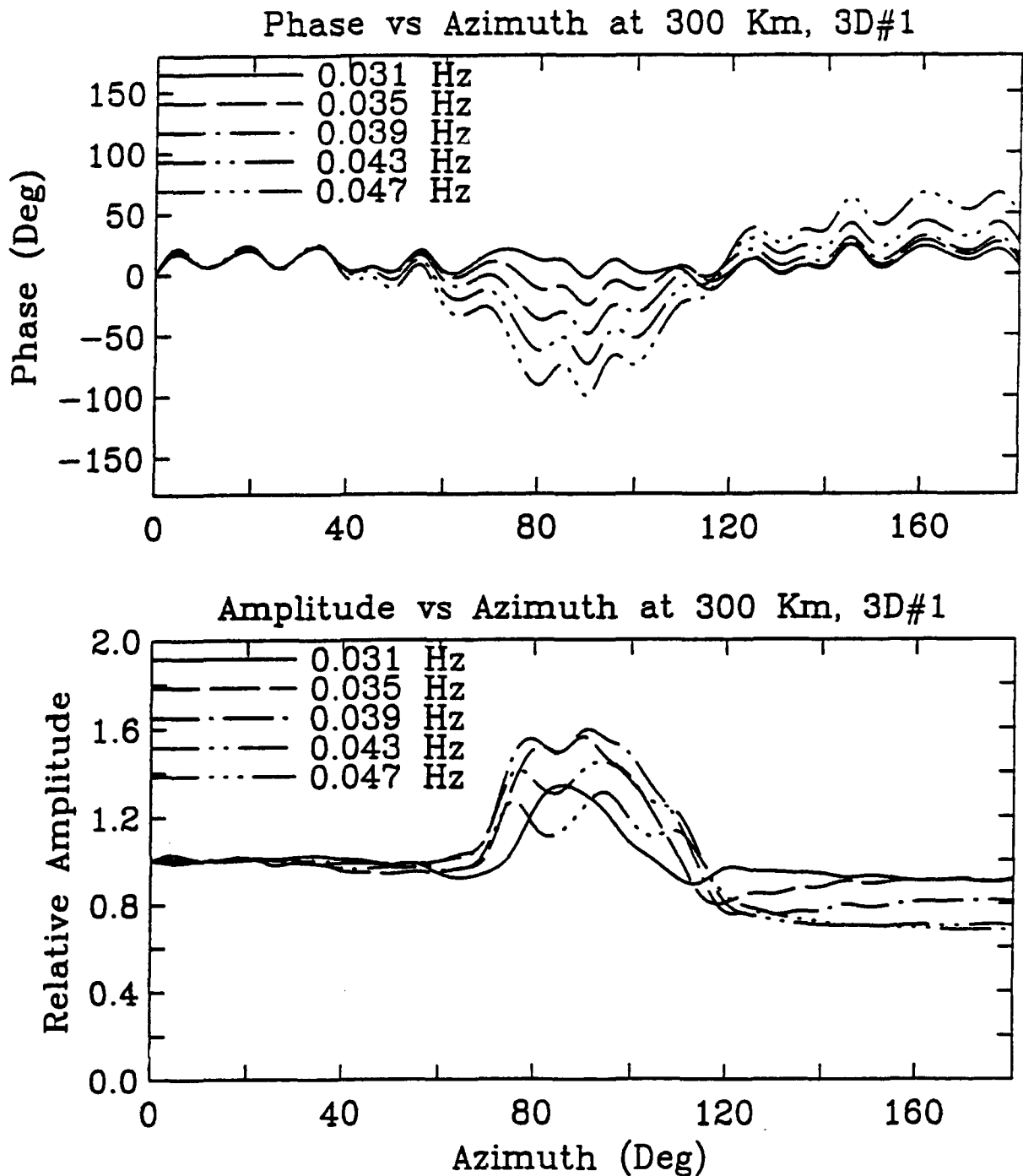


Figure 19A. The relative amplitude (bottom) and phase (top) for the Rayleigh wave at a distance of 300 km from the source in 3D simulation #1. Note the negative correlation between the large amplitude and phase (delayed) for azimuths to the east or west (90 degrees).

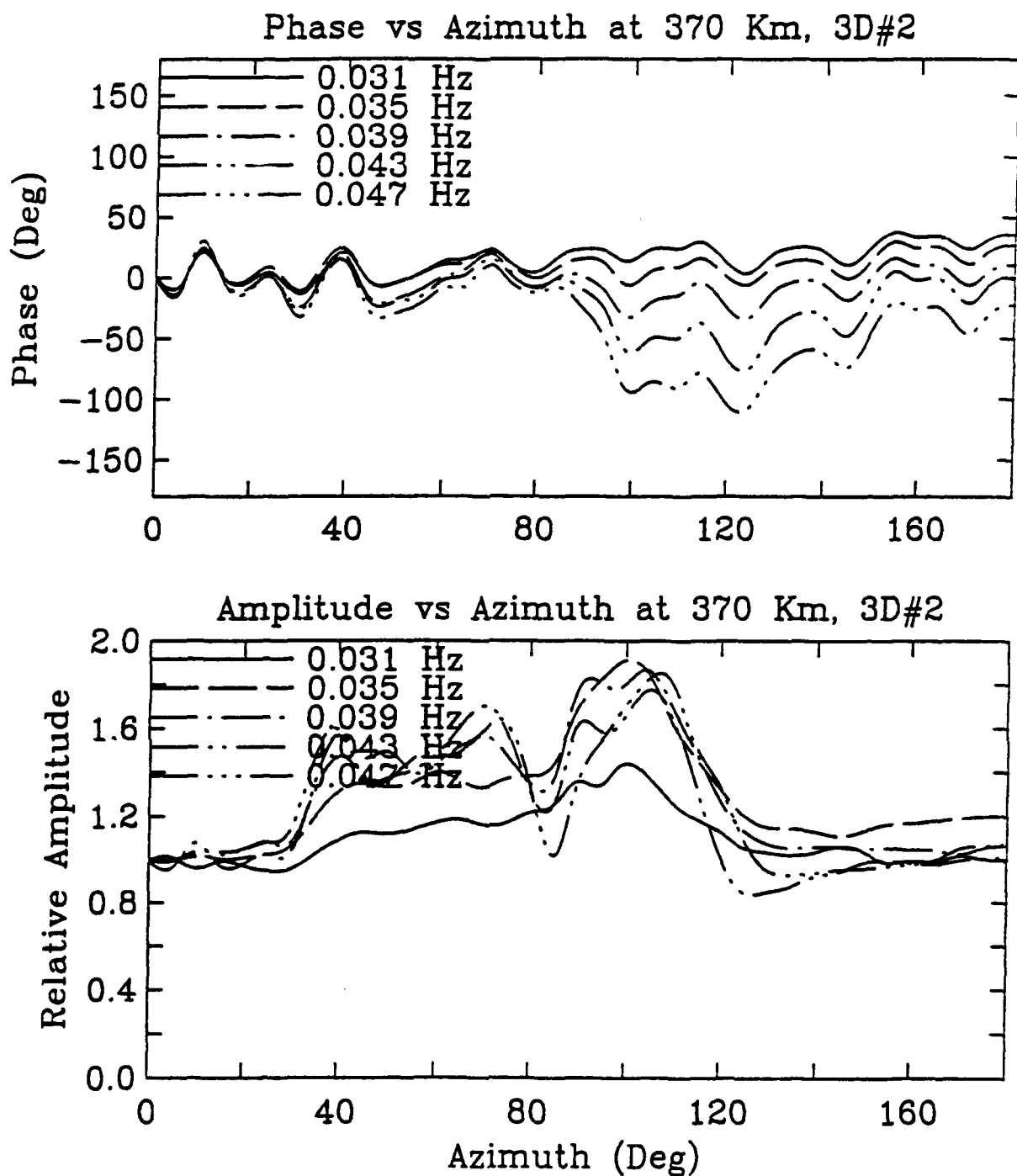


Figure 19B. The relative amplitude (bottom) and phase (top) for the Rayleigh wave at a distance of 370 km from the source in 3D simulation #2.

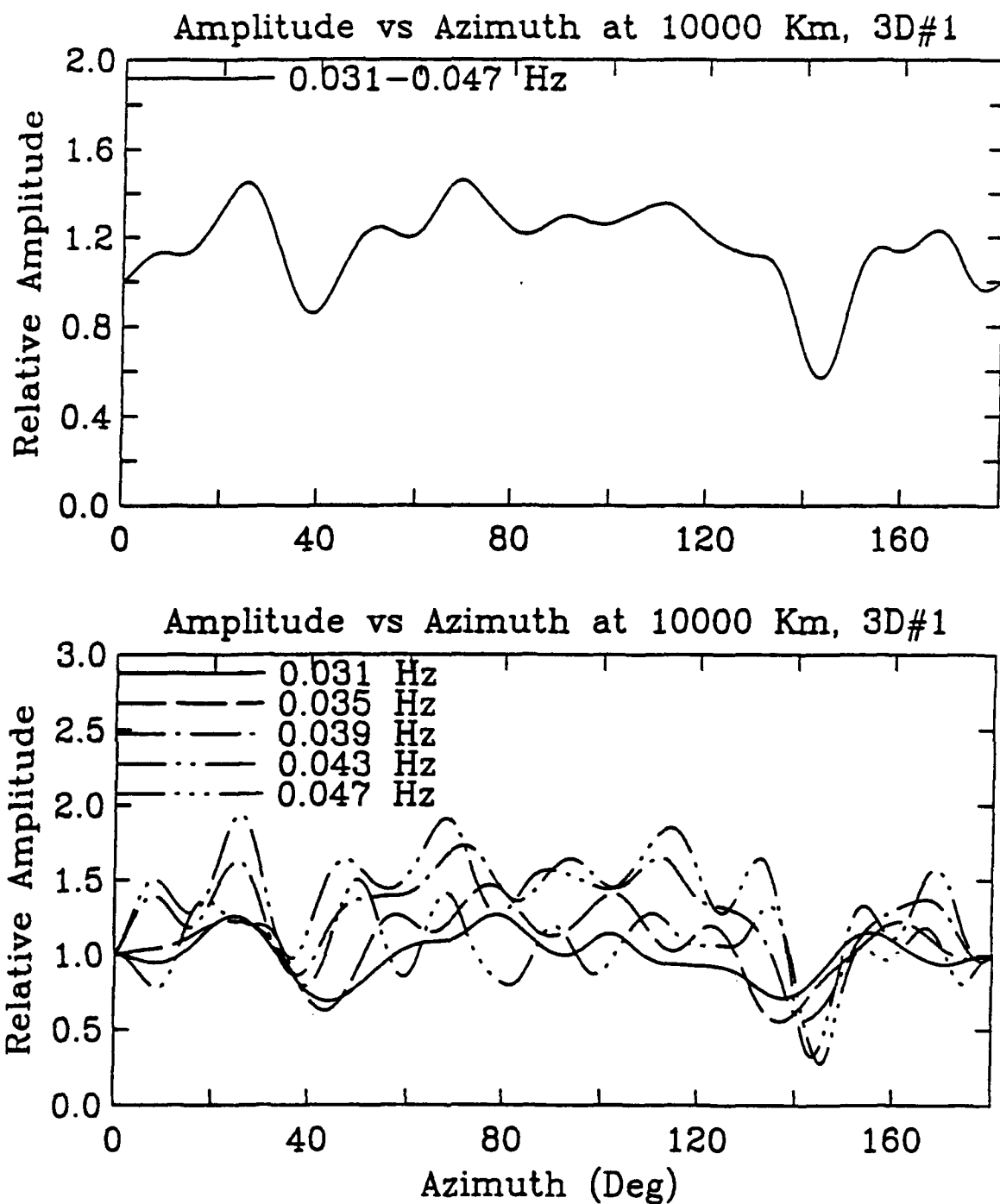


Figure 20A. Predicted teleseismic amplitudes from 3D simulation #1 as a function of azimuth using the Fresnel-Kirchoff integral to account for diffraction effects in the far-field. The average relative amplitude from 32 to 20 seconds period is at the top.

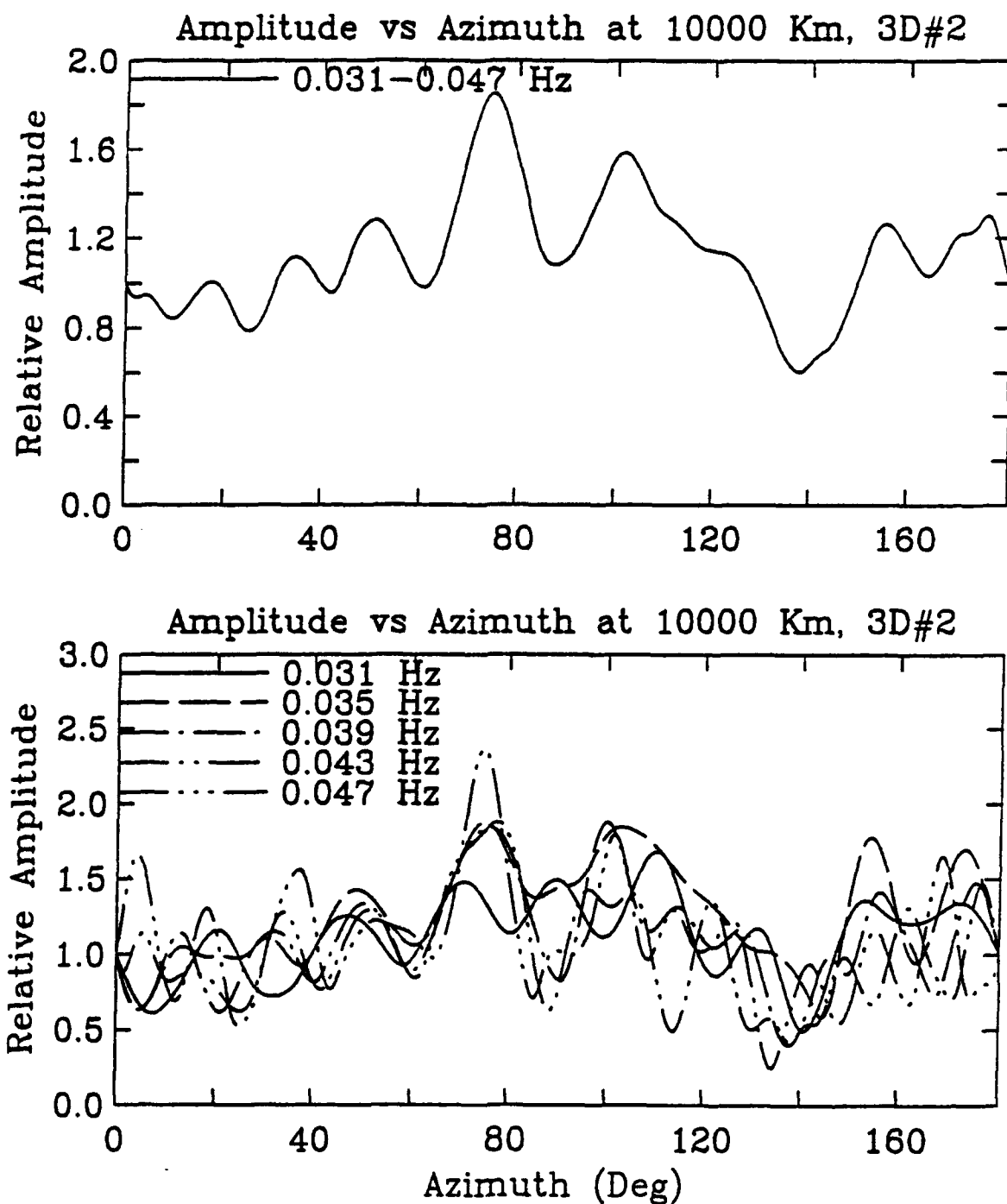


Figure 20B. Predicted teleseismic amplitudes from 3D simulation #2 as a function of azimuth using the Fresnel-Kirchoff integral to account for diffraction effects in the far-field. The average relative amplitude from 32 to 20 seconds period is at the top.

significantly. Similarly the results appear to be sensitive to details of the model and in particular the thickness of the crust in the region around the source. The local shallow model was poorly constrained.

6. CONCLUSIONS

We present results from a large 3D linear elastic finite difference calculation designed to simulate 20-40 second surface waves. Furthermore, we propose a procedure based on the Fresnel-Kirchoff integral for surface waves to continue the propagation from a 3D finite differences grid to teleseismic distances. The combination of these two techniques allow the seismologist to explore 3D near-source scattering effects on surface waves and project the results to teleseismic distances. 3D finite differences is a complete method that includes conversions, while the Fresnel-Kirchoff integral assumes a layered earth structure outside the 3D grid and accounts for far-field diffraction effects.

A 3D model for the velocity structure of the Aleutian arc has been used to predict teleseismic surface wave amplitudes from a shallow explosive source located on Amchitka Island. The predicted Rayleigh wave amplitudes show as much as a factor of two variation with azimuth. The amount of azimuthal variation is consistent with observations, although the observed pattern of the variation with azimuth is not reproduced exactly. Given that the shallow 3D velocity structure of the arc is not well known, it is encouraging that the simple 3D structure predicts an anomaly of about the right magnitude and similar character to that observed. Furthermore, the 3D model was restricted to model heterogeneity within 400 km of the Amchitka test site, and surface waves from Amchitka must propagate further along laterally varying structure to north American stations. It appears that much of the observed surface wave amplitude patterns from Amchitka island can be explained by refraction effects near the source region. The 3D modeling also predicts teleseismic Love waves from Rayleigh to Love scattering. Love waves were indeed observed by von Seggern (1973) from the MILROW collapse. These Love waves would be observed over limited azimuths, and with amplitudes approximately 1/3 to 1/4 the Rayleigh wave amplitude.

The dominant mechanism for the Rayleigh wave amplitude variation in the model appears to be lateral refraction due to a low velocity channel. This low velocity channel in the 20 to 30 second bandwidth is caused by a thick crust and low velocity sediments along the arc. The refraction is frequency dependent, and, because of the high velocity slab beneath the trench axis, this

region is a high velocity zone at periods longer than 35 seconds. Sources in and near the low velocity channel will appear to have a far-field radiation pattern at teleseismic distances because of the lateral refraction of energy along the channel. Similar focusing/defocusing effects have been modeled using ray tracing (von Seggern, *et al.*, 1975), Gaussian beams (Zeng, *et al.*, 1989) and a membrane vibration model of surface waves (Tanimoto, 1990). Ray tracing, Gaussian beams, and membrane models for surface wave refraction do not include mode conversions observed in the 3D elastic modeling. Rayleigh to Love wave scattering was strongest along the edges of the low velocity channel where lateral gradients are maximum and it is reasonable to assume that the Rayleigh to Love and Love to Rayleigh scattering phenomenon is common in regions of such strong lateral contrasts.

Assuming that near-source focusing/defocusing is a significant mechanism for the azimuthally dependent amplitude variations, we can begin to estimate the possible bias this may introduce into M_s or explosion moment determinations. The rms log-amplitude azimuthal variations predicted by 3D simulations #1 and #2 (top of Figures 20 A and B) are both 0.1 magnitude units. By contrast the rms station corrections of Stevens and McLaughlin (1989) (Figure 1) and McLaughlin, *et al.* (1986) (Figure 7) are about 0.2 magnitude units. The rms smoothed azimuthal variations (dashed lines in Figures 1 and 7) are about 0.12 to 0.14. Smoothing removes some of the scatter due to additional propagation and station effects far from the near-source region. If we assume that the smooth amplitude versus azimuth effects are caused by near-source focusing/defocusing then we can ask what possible bias may have been introduced into the estimated surface wave amplitude.

There are two possible sources of estimation bias. The first source comes from the non-uniform azimuthal sampling of data. Given the gaps in azimuth for which there is no or little data this source of bias can only be partly addressed since we were not able to reproduce the observed amplitude pattern. However, if we uniformly re-sample the smoothed amplitude patterns in Figures 1 and 7 there appears to be no bias due to the non-uniform sampling.

The second source of bias comes from log-amplitude averaging of the focusing/defocusing pattern as apposed to rms-amplitude averaging. By

definition the log-average of the station effects are zero as determined by Stevens and McLaughlin (1989) or McLaughlin, *et al.* (1986) in Figures 1 and 7 respectively. However, the use of log-averaging inherent in the statistical models that they used may lead to a bias in the estimated total energy in the presence of focusing/defocusing. If the smoothed amplitude variation is due to focusing/defocusing then total radiated surface wave energy integrated over azimuth should be invariant; the rms amplitude sampled uniformly over all azimuths should be unbiased (McLaughlin, 1986). Focusing/defocusing only redistributes energy from one azimuthal range to another and does not change the total energy radiated by the source. Assuming that the smoothed amplitude function is from near-source focusing/defocusing we can estimate the bias by resampling the smoothed amplitude functions and compute the rms amplitude. For the smoothed amplitude function in Figure 1, the uniformly sampled rms amplitude is 1.64 (0.21 magnitude units) larger than the baseline. Similarly, the estimated bias from Figure 7 is 1.47 or 0.17 magnitude units. Consequently, the log-average of surface wave amplitude as sampled by the WWSSN network is about 0.17 to 0.21 log-units smaller than it would be if the assumed near-source focusing/defocusing (dashed lines in Figures 1 and 7) were absent.

ACKNOWLEDGEMENTS

We wish to thank V. Cormier of the Univ. of Connecticut and K. Creager of the Univ. of Washington for kindly providing comments and subduction zone velocity models used in this study. This work was supported by DARPA/NMRO monitored by AFTAC under contract F-08606-89-C-0022.

REFERENCES

- Boyd, T. M. and K. C. Creager, (1991), "The Geometry of Aleutian Subduction: Three-Dimensional Seismic Imaging," *J. Geophys. Res.*, 96, pp. 2267-2291, February.
- Chiburis, E. F., and R. O. Ahner (1969), "A Location and Travel-Time Study of Aleutian Islands Explosions and Earthquakes," SDL Report 239, Teledyne Geotech, Alexandria, Va.
- Cormier, V. F. (1990) "Effects of a Descending Slab on Yield Estimates of Aleutian Nuclear Tests," GL-TR-90-0154,
- Davies, D. B. Julian (1972), "A Study of Short-Period P-Wave Signals from Longshot," *Geophys. J.*, 29, 185-202.
- Dziwonski, A. and D. Anderson (1983), "Travel Times and Station Corrections for P-Waves at Teleseismic Distances," *J. Geophys. Res.*, 88, 3295-3314.
- Engdahl, E. R. (1972), "Seismic Effects of the MILROW and CANNIKIN Nuclear Explosions," *Bull. Seism. Soc. Am.*, 62, 1411-1424.
- Jacob, K. H. (1972), "Global Tectonic Implications of Anomalous Seismic P Travel-Times from the Nuclear Explosion Longshot," *J. Geophys. Res.*, 77, 2556-2573.
- Lambert, D. G., D. H. von Seggern, S. S. Alexander, and G. A. Galt (1970), "The LONG SHOT Experiment, Comprehensive Analysis," SDL Report 234, Teledyne Geotech, Alexandria, Va.
- Klein, M. V. (1970). Optics, John Wiley and Sons Inc., N.Y., N. Y., 647 pages.
- Masse, R. P. (1971), "Radiation of Rayleigh Wave Energy from Nuclear Explosions and Earthquakes in Southern Nevada," SDL Report #266.
- Marshall, P. D., D. L. Springer, and H. C. Rodean (1979), "Magnitude Corrections for Attenuation in the Upper Mantle," *Geophys. J.*, 57, 609-638.
- McLaughlin, K. L., R. H. Shumway, R. O. Ahner, M. E. Marshall, T. W. McElfresh, and R. A. Wagner, (1986), "Determination of Event Magnitudes with Correlated Data and Censoring: a Maximum Likelihood Approach," TGAL-TR-86-01.
- McLaughlin, K. L. (1986), "Network Magnitude Variation and Magnitude Bias," *Bull. Seism. Soc. Am.* 76, 1813-1816.

- Given, J. W. and G. R. Mellman (1986), "Estimating Explosion and Tectonic Release Source Parameters of Underground Nuclear Explosions from Rayleigh and Love Wave Observations," AFGL-TR-86-0171, Sierra Geophysics, Wa.
- Page, E. A. (1972), "An Application of Ray-Tracing to Seismic Event Location," SDL Report 293, Teledyne Geotech, Alexandria, Va.
- Sleep, N. H. (1973), "Teleseismic P-wave Transmission Through Slabs," *Bull. Seism. Soc.*, 63, 1349-1373.
- Stevens, J. L. (1986a), "Estimation of Scalar Moments from Explosion-Generated Surface Waves," *Bull. Seism. Soc. Am.*, 76, 123-151.
- Stevens, J. L. (1986b), "Analysis of Explosion-Generated Rayleigh and Love Waves from East Kazakh, Amchitka, and Nevada Test Sites," AFGL-TR-86-0043.
- Stevens and McLaughlin (1989), "Analysis of Surface Waves from the Novaya Zemlya, Mururoa, and Amchitka Test Sites, and Maximum Likelihood Estimation of Scalar Moments from Earthquakes and Explosions," SSS-TR-89-9953.
- Stevens, J. L., S. M. Day, K. L. McLaughlin and B. Shkoller (1990), "Two-Dimensional Axisymmetric Calculations of Surface Waves Generated by an Explosion on an Island," S-CUBED Technical Report submitted to AFTAC,
- Tanimoto, T. (1990), "Modeling of Curved Surface Wave Paths: Membrane Surface Wave Synthetics," *Geophys. J. Int.* 102, 89-100.
- Toksoz, M. N. and H. H. Kehrner (1972), "Tectonic Strain Release Characteristics of CANNIKIN," *Bull Seism. Soc. Am.* 62, 1425-1438.
- von Seggern, D. H. and D. G. Lambert (1972), "Analysis of Teleseismic Data for the Nuclear Explosion MILROW," SDL Report 258, Teledyne Geotech, Alexandria, Va.
- von Seggern, D. H. (1973), "Seismic Surface Waves from Amchitka Island Test Site Events and Their Relation to Source Mechanism," *J. Geophys. Res.*, 78, 2467-2474.
- von Seggern, D. H., P. A. Sobel, and D. W. Rivers (1975), "Experiments in Refining Ms Estimates for Seismic Events," SDAC-TR-75-17.
- von Seggern, D. H., (1978), "Intersite Magnitude-Yield Bias Exemplified by the Underground Nuclear Explosions MILROW, BOXCAR and HANDLEY," SDAC-TR-77-4.

Willis, D. E, G. George, K. G. Poetzi, C. E. Saltzer, A. F. Shakal, R. Torfin, and T. L. Woodzick, (1972), "Final Report, Seismological and Related Effects of the CANNIKIN Underground Nuclear Explosion," Univ. of Wisconsin, COO-21380-9.

Zeng, Y., T.-L. Teng, and K. Aki (1989), "Surface Wave Ray Tracing and Ms:Yield Determination in a Laterally Heterogeneous Earth," AFGL-TR-0065.

APPENDIX I.

USE OF THE SURFACE-WAVE FRESNEL-KIRCHOFF INTEGRAL WITH FINITE DIFFERENCE CALCULATIONS

With a few justifiable assumptions we can compute far-field Rayleigh waves from the monitored displacements on a closed loop located on the surface of the 3D finite difference grid. We use the Fresnel-Kirchoff integral to compute the teleseismic response of the surface waves assuming that the region outside of the 3D grid is uniform or that the propagator from the outer edge of the 3D grid can be written simply as a phase factor and a geometrical spreading term.

For simplicity assume that the far-field propagator for the surface wave outside of the 3D finite difference grid is

$$P(|r-r'|) = \frac{e^{-ik|r-r'|}}{\sqrt{|r-r'|}}, \quad (1)$$

and that the surface wave amplitude incident of frequency, ω , incident upon a closed loop at the free surface, S , is given by $u(r', \omega) = A(r', \omega)\theta^i\phi(\omega)$, then the Fresnel-Kirchoff integral for the surface wave amplitude at a receiver location r outside of S is given by

$$u(r, \omega) = \frac{k}{2\pi} \int_S dl \, u(r', \omega) \frac{e^{-ik|r-r'|}}{\sqrt{|r-r'|}} (n_{r'} + n_r) \cdot n, \quad (2)$$

where n is the unit normal of the closed loop S (see Figure A1), $n_{r'}$ is the unit vector in the direction of propagation of the surface wave incident upon S , and n_r is the unit vector in the direction of the receiver from the loop, $n_r = \frac{r-r'}{|r-r'|}$.

The following derivation of Equation (2) for the surface wave "2D" geometry closely follows the derivation for the 3D scalar wave in Klein (1970). The Fresnel-Kirchoff integral (Eq 2) follows for any field that obeys the Helmholtz wave equation. We assume that two fields Φ and Ψ each obey the Helmholtz equation over a surface Σ ,

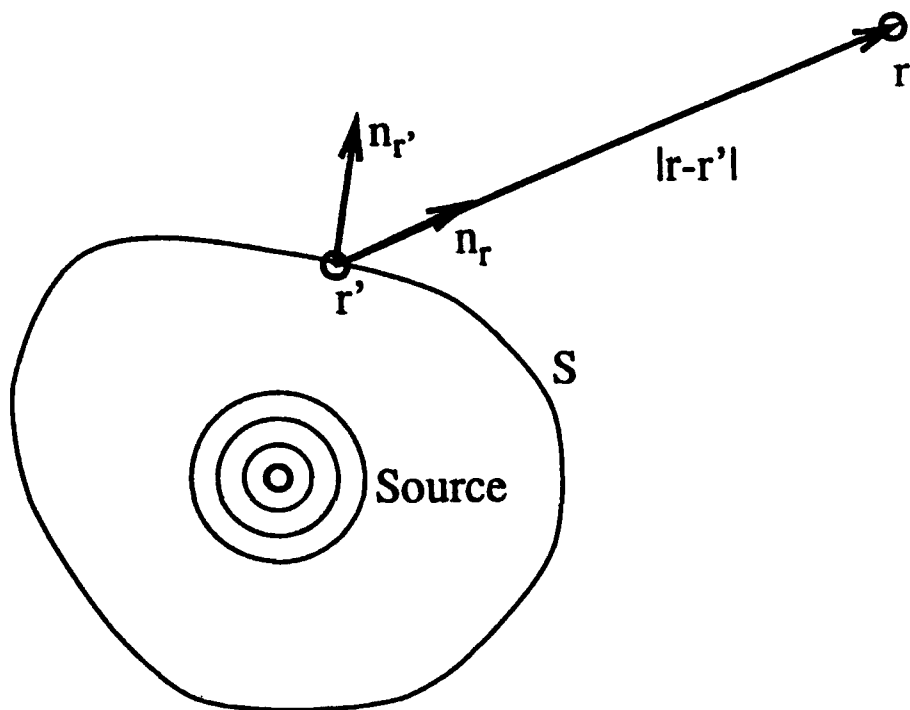


Figure A1. The wave field at r from the sources within S is given by Equation (2).

$$\nabla^2 \Phi - k^2 \Phi = 0, \quad (3a)$$

$$\nabla^2 \Psi - k^2 \Psi = \delta(r). \quad (3b)$$

We apply Green's theorem to the two fields,

$$\int_{\Sigma} (\Psi \nabla^2 \Phi - \Phi \nabla^2 \Psi) d^2 \sigma = \int_S \left(\Psi \frac{\partial \Phi}{\partial n} - \Phi \frac{\partial \Psi}{\partial n} \right) dl \quad (4)$$

where the surface Σ is bounded by the contour S formed by the two closed loops S_{outer} and S_{inner} (see Figure A2a). The area integral is zero since Ψ and Φ are solutions to Equation (3).

$$0 = \int_{S_{inner}} \left(\Psi \frac{\partial \Phi}{\partial n} - \Phi \frac{\partial \Psi}{\partial n} \right) dl + \int_{S_{outer}} \left(\Psi \frac{\partial \Phi}{\partial n} - \Phi \frac{\partial \Psi}{\partial n} \right) dl \quad (5)$$

We choose S_{inner} to be a circle of radius ϵ around the point r with normal directed toward r . $\Psi(r)$ is the Green's function for a source at r , and the integral over S_{inner} in the limit that ϵ goes to zero becomes, $-2\pi\Phi(r)$. With the result that for $k|r-r'| \ll 1$,

$$\Phi(r) = \frac{1}{2\pi} \int_{S_{outer}} \left(\Psi \frac{\partial \Phi}{\partial n} - \Phi \frac{\partial \Psi}{\partial n} \right) dl = \int_{S_{outer}} \left(\Psi \frac{\partial \Phi}{\partial n} - \Phi \frac{(-ik \cdot n_r) e^{-ik|r-r'|}}{\sqrt{|r-r'|}} \right) dl \quad (6)$$

If Φ has the form of a waveform incident on the loop S_{outer} then the normal derivative is approximated by the form of

$$\frac{\partial \Phi(r')}{\partial n} = -ikn \cdot n_r \Phi(r'), \quad (7)$$

where n_r is the direction of propagation of $\Phi(r')$. Therefore, we have the Fresnel-Kirchoff integral for the field at r given the field on a closed loop S enclosing r ,

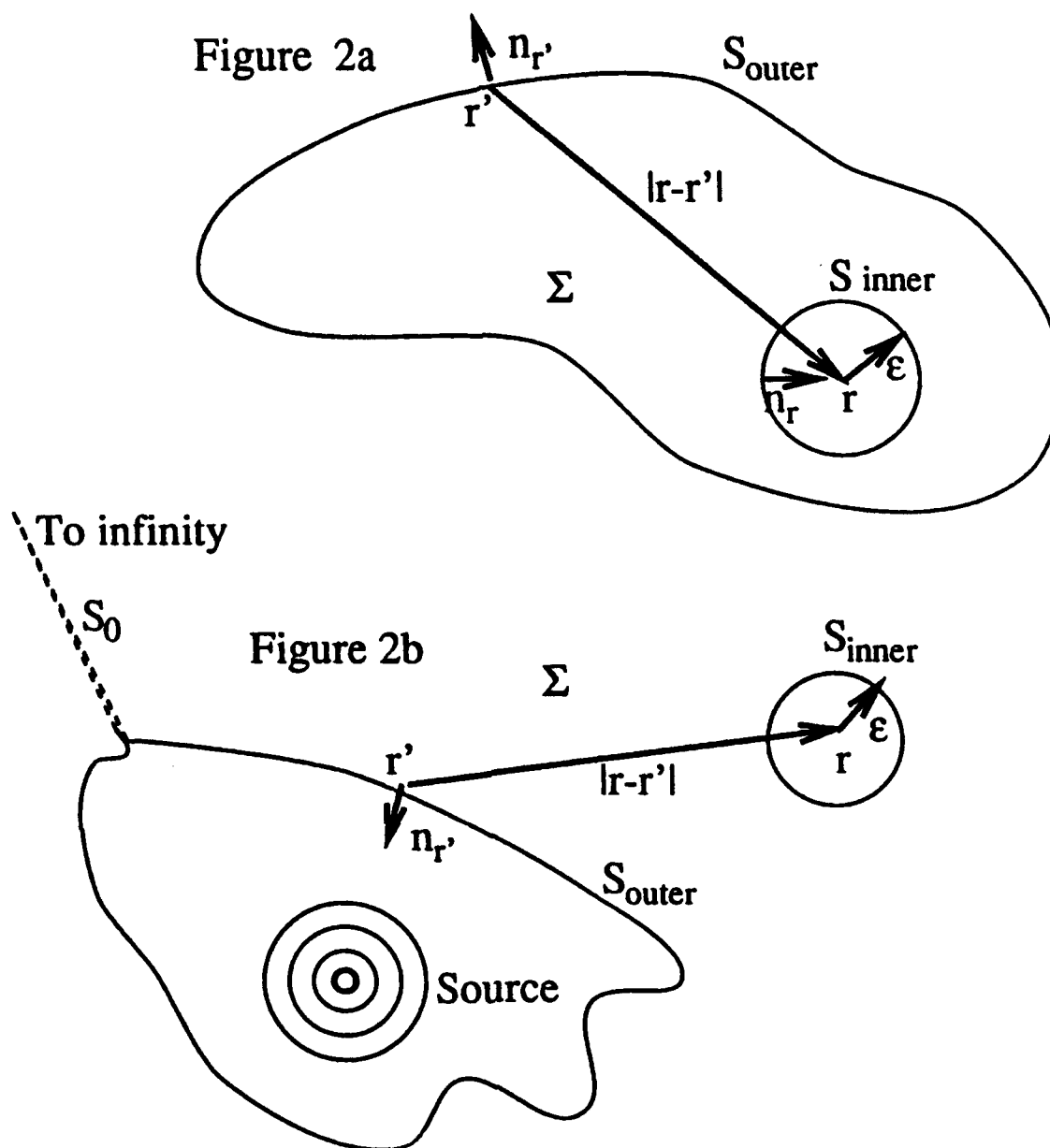


Figure A2. The region Σ is bounded by S_{inner} and closed loop S_{outer} (A2a above). Below, the loop S_{outer} is deformed around the source and scattering region with a section S_0 that goes to infinity such that Equation (9) becomes Equation (2) with a reversal in the sign of the normal on S_{outer} .

$$\Phi(r) = \frac{k}{2\pi} \int_S dl \Phi(r') \frac{e^{-ik|r-r'|}}{\sqrt{|r-r'|}} (n_{r'} \cdot n - n_r \cdot n). \quad (8)$$

In order to get the form of Equation (2) that is used for diffraction calculations we deform the outer loop to infinity and surround the source region by a loop as seen in Figure A2b connected to infinity by the segment S_0 . The contribution from the S_0 segment is zero. Note that this is equivalent to Figure 1 with the exception of the sign of the normal on the closed loop surrounding the source region and equation (8) becomes equation (2).

DISTRIBUTION LIST
FOR UNCLASSIFIED REPORTS
DARPA-FUNDED PROJECTS
(Last Revised: 26 Sep 89)

<u>RECIPIENT</u>	<u>NUMBER OF COPIES</u>
DEPARTMENT OF DEFENSE	
DARPA/NMRO ATTN: Dr. R. Alewine and Dr. A. Ryall 1400 Wilson Boulevard Arlington, VA 22209-2308	2
Defense Intelligence Agency Directorate for Scientific and Technical Intelligence Washington, D.C. 20340-6158	1
Defense Nuclear Agency Shock Physics Directorate/SD Washington, D.C. 20305-1000	1
Defense Technical Information Center Cameron Station Alexandria, VA 22314	2
DEPARTMENT OF THE AIR FORCE	
AFOSR/NP Bldg 410, Room C222 Bolling AFB, Washington, D.C. 20332-6448	1
AFTAC/STINFO Patrick AFB, FL 32925-6001	1
AFTAC/TT Patrick AFB, FL 32925-6001	3
AFWL/NTEG Kirkland AFB, NM 87171-6008	1
GL/LWH ATTN: Mr. James Lewkowicz Terrestrial Sciences Division Hanscom AFB, MA 01731-5000	1

DEPARTMENT OF THE NAVY

NORDA
ATTN: Dr. J. A. Ballard
Code 543
NSTL Station, MS 39529

1

DEPARTMENT OF ENERGY

Department of Energy
ATTN: Mr. Max A. Koontz (DP-331)
International Security Affairs
1000 Independence Avenue
Washington, D.C. 20585

1

Lawrence Livermore National Laboratory
ATTN: Dr. J. Hannon, Dr. S. Taylor, and Dr. K. Nakanishi
University of California
P.O. Box 808
Livermore, CA 94550

3

Los Alamos Scientific Laboratory
ATTN: Dr. C. Newton
P.O. Box 1663
Los Alamos, NM 87544

2

Sandia National Laboratories
ATTN: Mr. P. Stokes, Dept. 9110
P.O. Box 5800
Albuquerque, NM 87185

1

OTHER GOVERNMENT AGENCIES

Central Intelligence Agency
ATTN: Dr. L. Turnbull
OSI/NED, Room 5G48
Washington, D.C. 20505

1

U. S. Arms Control and Disarmament Agency
ATTN: Dr. M. Eimer
Verification and Intelligence Bureau, Rm 4953
Washington, D.C. 20451

1

U. S. Arms Control and Disarmament Agency
ATTN: Mr. R. J. Morrow
Multilateral Affairs Bureau, Rm 5499
Washington, D.C. 20451

1

U. S. Geological Survey
ATTN: Dr. T. Hanks
National Earthquake Research Center
345 Middlefield Road
Menlo Park, CA 94025

1

OTHER GOVERNMENT AGENCIES (continued)

U. S. Geological Survey MS-913 1
ATTN: Dr. R. Masse
Global Seismology Branch
Box 25046, Stop 967
Denver Federal Center
Denver, CO 80225

UNIVERSITIES

California Institute of Technology 1
ATTN: Dr. D. Harkrider
Seismological Laboratory
Pasadena, CA 91125

Columbia University 1
ATTN: Dr. L. Sykes
Lamont-Doherty Geological Observatory
Palisades, NY 10964

Cornell University 1
ATTN: Dr. M. Barazangi
INSTOC
Snee Hall
Ithaca, NY 14853

Harvard University 1
ATTN: Dr. J. Woodhouse
Hoffman Laboratory
20 Oxford Street
Cambridge, MA 02138

Massachusetts Institute of Technology 1
ATTN: Dr. T. Jordan
Department of Earth and Planetary Sciences
Cambridge, MA 02139

Southern Methodist University 2
ATTN: Dr. E. Herrin and Dr. B. Stump
Geophysical Laboratory
Dallas, TX 75275

DEPARTMENT OF DEFENSE CONTRACTORS

Center for Seismic Studies ATTN: Dr. C. Romney and Mr. R. Perez 1300 N. 17th Street, Suite 1450 Arlington, VA 22209	2
ENSCO, Inc. ATTN: Dr. R. Kemerait 445 Pineda Court Melbourne, FL 32940-7508	1
Pacific Sierra Research Corp. ATTN: Mr. F. Thomas 12340 Santa Monica Boulevard Los Angeles, CA 90025	1
Science Applications International Corporation ATTN: Document Control (Dr. T. Bache, Jr.) 10260 Campus Point Drive San Diego, CA 92121	1
Science Horizons ATTN: Dr. T. Cherry and Dr. J. Minster 710 Encinitas Blvd. Suite TOI Encinitas, CA 92024	2
S-CUBED, A Division of Maxwell Laboratories, Inc. ATTN: Dr Jeff Stevens P.O. Box 1620 La Jolla, CA 92038-1620	1
Sierra Geophysics, Inc. ATTN: Dr. R. Hart and Dr. G. Mellman 11255 Kirkland Way Kirkland, WA 98033	2

OTHER DISTRIBUTION

To be determined by the project office	7
--	---

TOTAL 50